## Template for Preparation of Manuscripts for Nano Research

This template is to be used for preparing manuscripts for submission to *Nano Research*. Use of this template will save time in the review and production processes and will expedite publication. However, use of the template is not a requirement of submission. Do not modify the template in any way (delete spaces, modify font size/line height, etc.). If you need more detailed information about the preparation and submission of a manuscript to *Nano Research*, please see the latest version of the Instructions for Authors at <a href="http://www.thenanoresearch.com/">http://www.thenanoresearch.com/</a>.

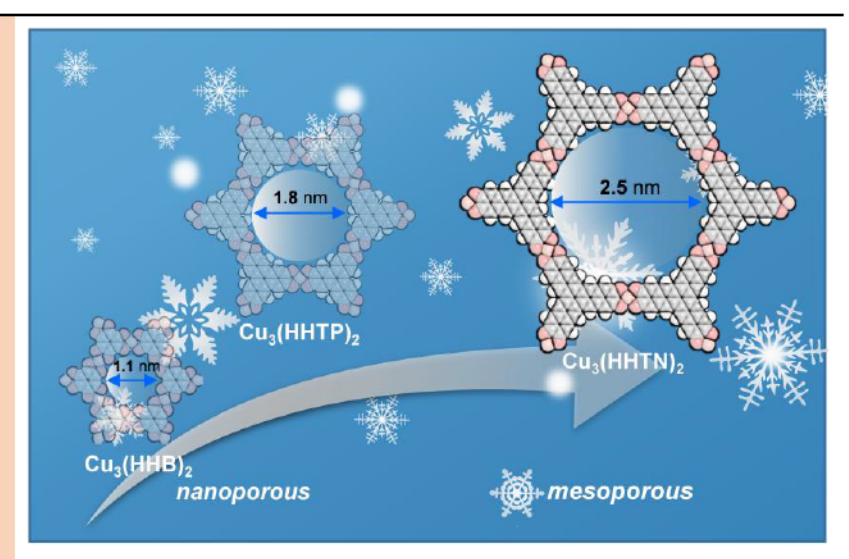
#### TABLE OF CONTENTS (TOC)

Authors are required to submit a graphic entry for the Table of Contents (TOC) in conjunction with the manuscript title. This graphic should capture the readers' attention and give readers a visual impression of the essence of the paper. Labels, formulae, or numbers within the graphic must be legible at publication size. Tables or spectra are not acceptable. Color graphics are highly encouraged. The resolution of the figure should be at least 600 dpi. The size should be at least 50 mm × 80 mm with a rectangular shape (ideally, the ratio of height to width should be less than 1 and larger than 5/8). One to two sentences should be written below the figure to summarize the paper. To create the TOC, please insert your image in the template box below. Fonts, size, and spaces should not be changed.

Two-dimensional d- $\pi$  conjugated metal-organic framework based on hexahydroxytrinaphthylene

Zheng Meng and Katherine A. Mirica\*

Dartmouth College, United States



A novel d- $\pi$  conjugated two-dimensional metal-organic framework Cu<sub>3</sub>(HHTN)<sub>2</sub> using a new ligand 2,3,8,9,14,15-hexahydroxytrinaphthylene was synthesized. The resulting material has a pore aperture of 2.5 nm, tunable electrical conductivity, and temperature-dependent band gap ranging from 0.75 to 1.65 eV.

Provide the authors' webside if possible.

Author 1, webside 1

Author 2, http://www.miricagroup.com





# Two-dimensional d- $\pi$ conjugated metal-organic framework based on hexahydroxytrinaphthylene

Zheng Meng<sup>1</sup> and Katherine A. Mirica<sup>1</sup>( )

<sup>1</sup>Department of Chemistry, Burke Laboratory, 41 College Street, Dartmouth College, Hanover, NH 03755, United States

© Tsinghua University Press and Springer-Verlag GmbH Germany, part of Springer Nature 2018

Received: day month year / Revised: day month year / Accepted: day month year (automatically inserted by the publisher)

#### **ABSTRACT**

The development of new two-dimensional (2D) d- $\pi$  conjugated metal-organic frameworks (MOFs) holds great promise for the construction of a new generation of porous and semiconductive materials. This paper describes the synthesis, structural characterization, and electronic properties of a new d- $\pi$  conjugated 2D MOF based on the use of a new ligand 2,3,8,9,14,15-hexahydroxytrinaphthylene. The reticular self-assembly of this large  $\pi$ -conjugated organic building block with Cu(II) ions in a mixed solvent system of 1,3-dimethyl-2-imidazolidinone (DMI) and H<sub>2</sub>O with the addition of ammonia water or ethylenediamine leads to a highly crystalline MOF Cu<sub>3</sub>(HHTN)<sub>2</sub>, which possesses pore aperture of 2.5 nm. Cu<sub>3</sub>(HHTN)<sub>2</sub> MOF shows moderate electrical conductivity of 9.01×10<sup>-8</sup> S/cm at 385 K and temperature-dependent band gap ranging from 0.75 to 1.65 eV. After chemical oxidation by I<sub>2</sub>, the conductivity of Cu<sub>3</sub>(HHTN)<sub>2</sub> can be increased by 360 times. This access to HHTN based MOF adds an important member to previously reported MOF systems with hexagonal lattice, paving the way towards systematic studies of structure–property relationships of semiconductive MOFs.

#### **KEYWORDS**

two-dimensional, metal-organic framework, trinaphthylene, conductive MOF

#### 1 Introduction

The recent emergence of conductive metal-organic frameworks (MOFs)1-4 offers opportunities for molecular engineering of novel functions in electronics,5-7 chemical sensing,8-19 magnetics,20-24 catalysis,25-30 and energy storage.31-37 Characterized by well-defined modular structure accessible through bottom-up self-assembly, this class of materials provides approach towards fundamental multifunctional materials design.4 The attractive feature of conductive MOFs centers on their elegant combination of intrinsic porosity and electrical conductivity, which differentiates them from conventional insulating MOFs.8-10 Creation of efficient and long-range charge transport pathway typically relies on the construction of 2D MOFs comprising extended  $\pi$ -conjugated organic building blocks interconnected with transition metals,3,38 where the p-d orbital coupling between the ligand and metal node facilitates "through-bond" charge transport.3-4, 39 Following this strategy, 2D MOFs with conductivity from semiconductive to metallic have been developed. Despite the applied and fundamental potential of 2D d-π conjugated MOFs, in most cases, strategic modulation of both the conductivity and porosity has remained limited, and the design principles for engineering conductivity and band gap have been largely unexplored.

With a few exceptions, <sup>16, 24, 28-29, 40</sup> the existing 2D conductive MOFs rely mainly on two types of organic building blocks: hexasubstituted benzene (HXB)<sup>5, 41-44</sup> and hexasubstituted triphenylene (HXTP, X=NH, O, S, Se). <sup>3-4, 9, 25, 38, 42, 45-49</sup> These redox-active ligands with ortho-positioned N, O, S, or Se donor

atoms

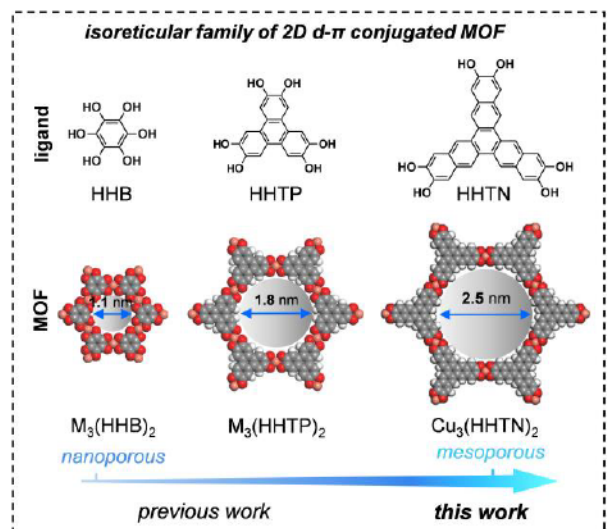


Figure 1. The isoreticular family of 2D d- $\pi$  conjugated MOFs comprising three MOFs synthesized from a series of analogous hexasubstituted aromatic ligands. can coordinate to a variety of late-transition-metal nodes capable of providing octahedral or square-planar coordination geometry, resulting in nanoporous 2D MOFs with pore diameters ranging between 1–2 nm. The increasing demand for the development of novel conductive MOFs, as well as the need for improving understanding of their structure–property relationships, can significantly benefit from the systematic expansion of the known structural topology of the Kagome lattice, with electronic structure,

Nano Res.

pore size and other properties controlled in an atomically precise manner. The construction of isoreticular MOFs series, in which the MOFs share the same 2D topology, but different functionalities and dimensions, has proven to be a powerful strategy to probe the structure–property relationships. <sup>50-53</sup> This strategy leverages on the fact that the structure of the organic ligand can directly influence sizes of pore aperture and efficiency of the electronic communication between ligand and metal nodes. <sup>3-4, 39, 54</sup>

In this paper, we describe the synthesis, structural characterization, and properties of a new d- $\pi$  conjugated 2D MOF based on a new ligand-2,3,8,9,14,15-hexahydroxytrinaphthylene (HHTN)-the  $\pi$ -extended analog 1,2,3,4,5,6-hexahydroxybenzene (HHB) and 2,3,6,7,10,11-hexahydroxytrinaphthylene (HHTP). The reticular self-assembly of this large  $\pi$ -conjugated organic building block with Cu(II) ions leads to a MOF Cu<sub>3</sub>(HHTN)<sub>2</sub> with pore aperture up to 2.5 nm, pushing the 2D  $\pi$ -conjugated semi-conductive MOF into the mesoporous realm. Cu<sub>3</sub>(HHTN)<sub>2</sub> showed moderate electrical conductivity of 9.01×10<sup>-8</sup> S/cm at 385 K and temperature-dependent band gaps ranging from 0.75 to 1.65 eV. After chemical oxidation by I2, the conductivity of Cu3(HHTN)2 can be increased by 360 times, highlighting the tunability of the property. The access to HHTN-based MOF adds an important member to previously reported HHB- and HHTP- based MOFs, thus generating the first isoreticular family of 2D d- $\pi$  conjugated MOFs comprising at least three systematically expanded lattice structures. This achievement can promote comparative fundamental study of structure-property relationship in 2D d- $\pi$ conjugated MOFs, and is poised to pave the ways for new opportunities in thermal switching, sensing, and energy-related applications.

#### 2 Results and discussion

Scheme 1. The synthesis and chemical structure of Cu<sub>3</sub>(HHTN)<sub>2</sub> MOF.

#### 2.1 MOF synthesis

The synthesis of HHTN ligand relied on the formation trinaphthylene core under a triple Ni(cod)2 promoted Yamamoto-type coupling cyclization<sup>55</sup> followed by demethylation generate novel compound 2,3,8,9,14,15-hexahydroxytrinaphthylene in 89% yield (see SI for synthetic details). Cu(II) was selected as the bridging metal node (Scheme 1) to enable access to a third member of the isoreticular series of Cu-based 2D MOF with Kagome lattice. A series of synthetic conditions, including the effects of solvent, concentration, and base, were tested (See Section 2.2 in Supporting information). Aqueous solvothermal conditions typically employed for the synthesis of HHB and HHTP based MOFs turned out to be unadaptable, likely due to limited solubility of HHTN in H2O. We found that the addition of base (ammonia water or ethylenediamine) was necessary for the deprotonation of the catechol to facilitate the coordination. The mixed solvent system of DMI and H<sub>2</sub>O, which moderately solubilized HHTN, produced the desired product with good crystallinity in the presence of ammonia water (See Table S1 and Figure S7).

#### 2.2 Structural characterization

The formation of Cu<sub>3</sub>(HHTN)<sub>2</sub> MOF with the structure consistent with that in Figure 2a was confirmed by powder X-ray diffraction (PXRD). As shown in Figure 2b, the bulk material Cu<sub>3</sub>(HHTN)<sub>2</sub> showed prominent peaks at  $2\theta = 3.49^{\circ}$ , 6.95°, 9.17°, 12.02°, and 27.13°, corresponding to the diffractions of [100], [200], [210], [220], and [001] planes, respectively. From peaks at these values, a structural pore diameter (defined by the distance of the hydrogen atoms at the opposite sides of the hexagon) of 2.5 nm was deduced based on Bragg's law. This value is much larger than the pore diameter HXTP- and HXB-based MOFs, which have been reported to be 1.8-2.09, 31, 45-46 and 0.8 nm, 34, 43 respectively. The presence of the sharp diffraction peaks from the planes perpendicular to ab planes indicated the long-range hexagonal in-plane arrangement. The diffraction peak of [001] at 27.13° was relatively weak, demonstrating a diminished long-range order along the *c* direction. The interlayer spacing  $d_{001}$  calculated from the [001] diffraction was 3.29 Å, which is similar with that of the Cu<sub>3</sub>(HHTP)<sub>2</sub> ( $d_{001}$ = 3.3 Å)<sup>13</sup>, <sup>38</sup>, but larger than that of Cu<sub>3</sub>(HHB)<sub>2</sub> ( $d_{001}$ = 2.96 Å).<sup>44</sup>

To ascertain the packing mode, three possible types of structural models, including fully eclipsed, slipped parallel, and staggered packing, were computationally examined for  $Cu_3(HHTN)_2$ . DFT optimization was used for the fully eclipsed model to optimize the atomic coordinates. To determine the propensity for slip plane, 78 structures with different ab-plane displacements were generated from the fully eclipsed model. The free energies of the resulting structures were analyzed and compared using single-point energy calculations based on molecular force field COMPASS II (ultrafine level) with FORCIET modular implemented in Materials Studio. As shown in **Figure 2c**, for  $Cu_3(HHTN)_2$  MOF, the minimum of the potential energy surface corresponds to a displacement ( $\Delta a$  and  $\Delta b$ ) of 1.4–1.5 Å along the a axis and 0.7–0.8 Å along the b axis between the adjacent two layers (**Figure 2d**).

The same method was also used for the determination of the displacement for Cu<sub>3</sub>(HHB)<sub>2</sub> and Cu<sub>3</sub>(HHTP)<sub>2</sub>, which have also been previously characterized to have slipped parallel packing modes.<sup>44, 47, 56</sup> The results showed that displacements along a and b axes in the most thermodynamically stable lattices were  $\Delta a = 2.5$  Å,  $\Delta b = 1.2$  Å for Cu<sub>3</sub>(HHB)<sub>2</sub> and  $\Delta a = 3.7$  Å,  $\Delta b = 3.0$  Å for

Nano Res.

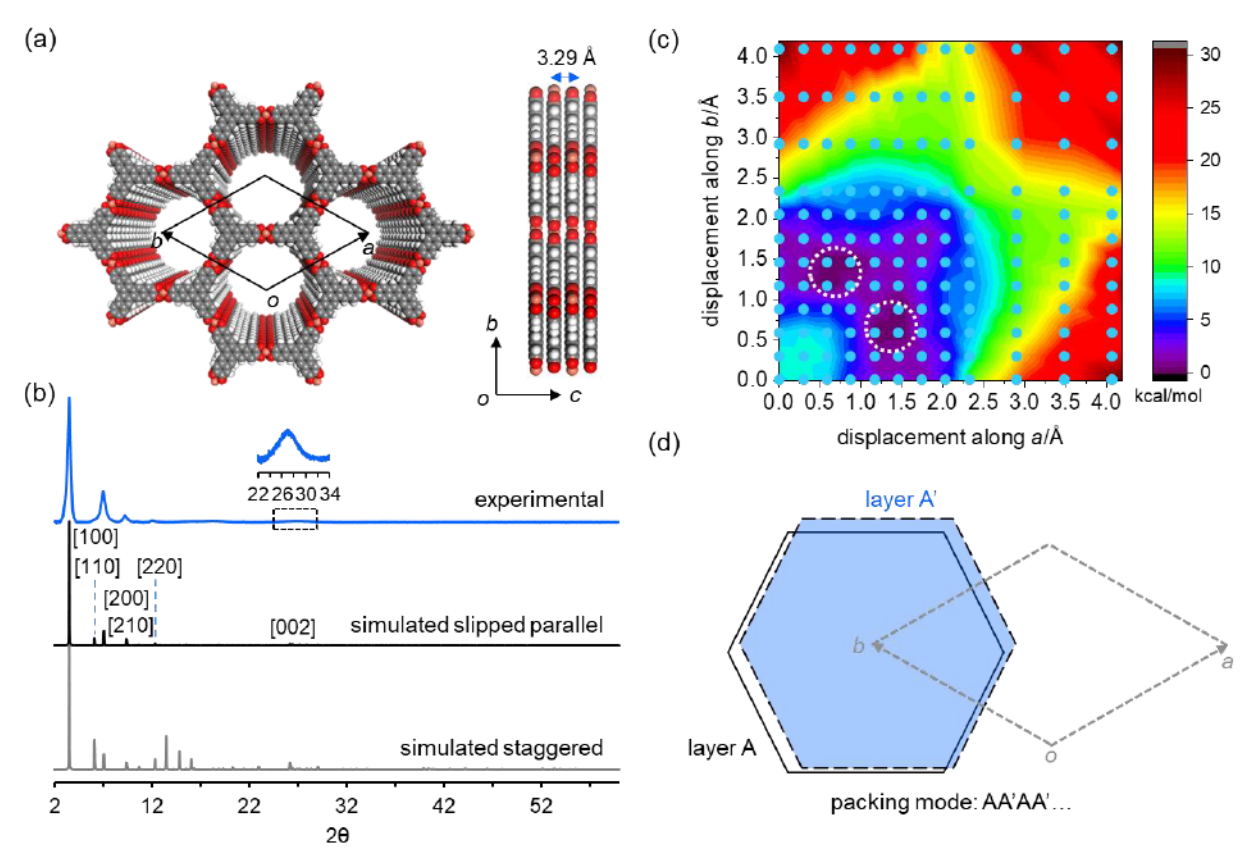


Figure 2. (a) Top and side view of  $Cu_3(HHTN)_2$  MOF. (b) Experimental (blue line) and simulated PXRD pattern of  $Cu_3(HHTN)_2$  MOF with slipped parallel (black line) and staggered packing (grey line). (c) Contour map of the potential energy surface for  $Cu_3(HHTN)_2$  MOF generated by different translations along a and b axis. The energy per unit cell at the minimum has been normalized to zero. (d) Representation of the relative displacement of the two adjacent layers in  $Cu_3(HHTN)_2$ .

Cu<sub>3</sub>(HHTP)<sub>2</sub> (**Figure S14-S15**). This comparison illustrated that the relative displacement in these three MOFs ( $\Delta a/a$  and  $\Delta b/b$ ) contracts with the extension of the  $\pi$ -system of the ligand. This result suggests that  $\pi$ - $\pi$  interactions between adjacent layers gradually increase with the expansion of the ligand and have a dominant effect on the interlayer packing, considering that interlayer displacement is a function of the balance between the attractive  $\pi$ - $\pi$  interaction, interlayer metal-oxygen interaction, and electrostatic repulsion resulting from oxygens and metal centers in the adjacent layers.<sup>57</sup>

Cu<sub>3</sub>(HHTN)<sub>2</sub> exhibited a reversible nitrogen sorption isotherm curves with a Brunauer–Emmett–Teller surface area of 486 m<sup>2</sup> g<sup>-1</sup> (**Figure S24**), which is 3.4 times greater than that of Cu<sub>3</sub>(HHB)<sub>2</sub><sup>44</sup> and 1.7 times greater than that of Cu<sub>3</sub>(HHTP)<sub>2</sub>.<sup>58</sup> The distribution of accessible pore size derived from the gas adsorption centered around 2 nm. This value is smaller than that deduce from PXRD analysis, which can be due to the slipped parallel packing that reduces the accessible size of the channel, and the possible presence of counter ions and other adsorbed species (e.g., solvent molecules).

#### 2.3 Morphological characterization

Analysis of Cu<sub>3</sub>(HHTN)<sub>2</sub> scanning electron microscopy (SEM) showed sub-micrometer sized rods (**Figure 3a, 3b**). Transmission electron microscopy (TEM) imaging of Cu<sub>3</sub>(HHTN)<sub>2</sub> revealed sheet-like morphology with multiple layers (**Figure 3c**). TEM image at higher magnification at the edge of the MOF sheet allowed the visualization of regular stripes with a spacing of 1.29 nm corresponding to [200] facets (**Figure 3d**); this value is in good agreement with the value obtained from the PXRD analysis

 $(d_{200}$ =1.27 nm). The ease of visualization of the [200] facets compared with facets aligned in other directions is likely due to the preferential orientation of the observed crystallite on the TEM grid or acquisition conditions for the TEM image.<sup>38</sup> These imaging results further evidenced the formation of  $Cu_3(HHTN)_2$  MOF with high structural regularity at micro and nanoscale.

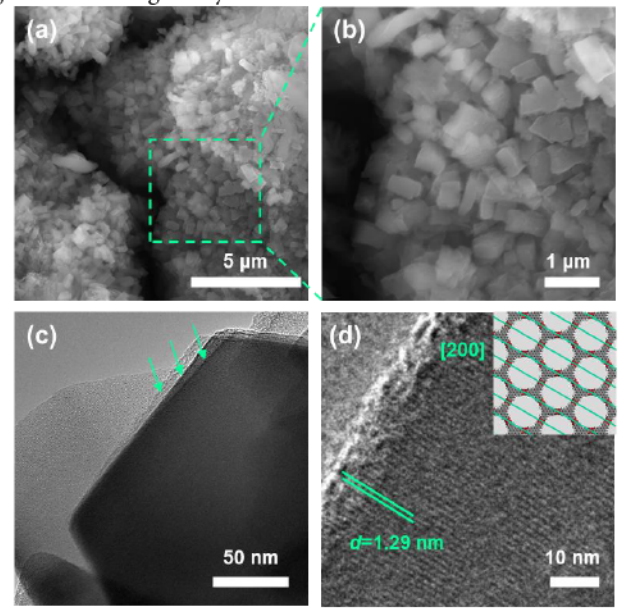


**Figure 3.** (a)–(b) SEM images of MOF Cu<sub>3</sub>(HHTN)<sub>2</sub> at different magnifications. (c) TEM of Cu<sub>3</sub>(HHTN)<sub>2</sub> exfoliated by sonication in acetone showing sheets with multiples layers. (d) The visualization of [200] facets by TEM.

#### 2.4 Chemical analysis

Energy dispersive spectroscopy (Figure S21) conducted for corresponding areas showed the presence of C, O, and Cu elements, consistent with the desired composition of Cu<sub>3</sub>(HHTN)<sub>2</sub> MOF. High-resolution scans by X-ray photoelectron spectroscopy of the O 1s showed three peaks with binding energies at 284.7 eV, 286.2 eV, and 288.1 eV (Figure S10a), ascribed to carbon in the environments of C-C, C-O, and C=O. The 1:1 relative intensity of the C-O to C=O suggested that the oxidation state of the ligand is likely to exist as tri(semiquinone) form, corresponding to -3apparent charge. This analysis was consistent with the analysis of the high-resolution scan of O 1s range, which can be fitted to two peaks for C-O and C=O at binding energies of 531.5 and 532.9 eV in an intensity ratio of 48:52 (Figure S10c). High-resolution scan of Cu 2p range can be deconvoluted into two components at binding energies of 933.5 and 935.3 eV with an intensity ratio of 41:59 (Figure S10d), suggesting that Cu in Cu<sub>3</sub>(HHTN)<sub>2</sub> may exist in a mixed oxidation state9 of Cu(I) and Cu(II) in a ratio of 2:3. The presence of Cu(II) was also confirmed by the electron paramagnetic resonance spectroscopy in which a strong metal-centered radical ascribed to paramagnetic Cu(II) was observed (Figure S22). The above analysis suggested that the skeleton of the MOF with a formula Cu<sub>3</sub>(HHTN)<sub>2</sub> is likely to possess a net charge of nearly -1. The framework may achieve charge neutrality by the incorporation of the counter ions, that are very likely from the NH<sub>4</sub><sup>+</sup> introduced from the MOF synthesis, as suggested by the presence of N in XPS (Figure S10b).

#### 2.5 Electronic properties and tunability

Given the d- $\pi$  conjugated structure of Cu<sub>3</sub>(HHTN)<sub>2</sub> MOF, we proceeded to examine its electronic properties. UV-vis-NIR spectroscopy revealed a relatively broad absorption band, which tailed into the NIR region beyond 850 nm (**Figure 4a**). The optical

band gap was estimated to be 1.61 eV based on the value of absorption edge (inset in Figure 4a). The bulk conductivity of Cu<sub>3</sub>(HHTN)<sub>2</sub> MOF was measured on a pressed pellet with a thickness of ~1 mm by a two-point method, which gave a value of 9.55×10<sup>-10</sup> S cm<sup>-1</sup> at room temperature. Variable temperature conductivity measurement showed that increasing the temperature from 298 K to 385 K increased the conductivity to 9.01×10<sup>-8</sup> S cm<sup>-1</sup> (Figure 4b), which is a 94-fold increase within a  $\Delta T$  of 87 K. The Arrhenius fit of conductivity to temperature revealed two distinct regions (Figure 4c), demonstrating a notable temperature dependence of band gap within the tested temperature range. The activation energy for the transport of charge carriers in Cu<sub>3</sub>(HHTN)<sub>2</sub> MOF determined at a lower temperature range of 298-319 K (zone I in Figure 4c) was 827 meV (Figure S27), corresponding to a thermal bandgap of 1.65 eV; this bandgap value in good agreement with the value estimated by UV-vis-NIR spectroscopy. In the higher temperature range of 324-385 K (zone II in Figure 4c), a smaller thermal band gap of 0.75 eV was found (Figure S27).

Although temperature-dependence of band gap has been well documented in traditional inorganic semiconductors,59-64 and has recently been recognized in organic semiconductors<sup>65-66</sup> and such perovskites,67 Si, Ge, PEDOT as  $(C_4H_9NH_3)_2(CH_3NH_3)_{n-1}Pb_nI_{3n+1}$ , this property has not been extensively characterized in semiconducting reticular materials. Theoretically, the energy barrier for charge transport is ascribed to both the intrinsic charge transport within the crystallite (intraparticle transport) and charge hopping over grain boundaries (interparticle transport) in the bulk measurement.<sup>43</sup> The relatively minor contribution from grain boundary effects to the total energy barrier of charge transport, as evidenced by the fact that the thermal band gap obtained at room temperature is only slightly

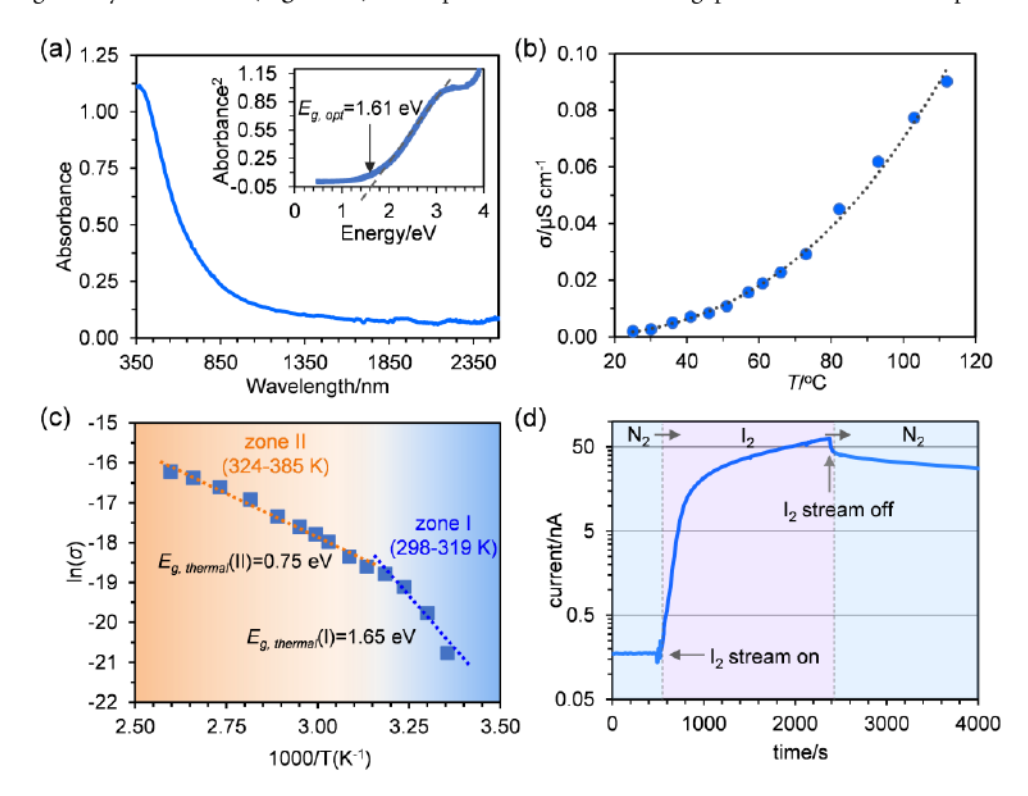


Figure 4. (a) UV-vis-NIR spectrum of Cu<sub>3</sub>(HHTN)<sub>2</sub> at room temperature. The inset is the plot of absorbance square vs energy of the UV-vis-NIR spectrum. (b) The electrical conductivity of Cu<sub>3</sub>(HHTN)<sub>2</sub> as a function of temperature at the range of 298-385 K. (c) The Arrhenius fitting of conductivity to temperature showed two distinct zones for Cu<sub>3</sub>(HHTN)<sub>2</sub>. (d) The change in the current of a Cu<sub>3</sub>(HHTN)<sub>2</sub> based resistor upon I<sub>2</sub> doping (~400 ppm) at room temperature.

higher than optical band gap for Cu<sub>3</sub>(HHTN)<sub>2</sub>, suggested that the temperature-dependence of band gap was mainly caused by intrinsic changes in charge-transport barrier.<sup>68-69</sup>

Compared to Cu<sub>3</sub>(HHTP)<sub>2</sub>8, 13, 38, 47 and Cu<sub>3</sub>(HHB)<sub>2</sub>44 MOFs, Cu<sub>3</sub>(HHTN)<sub>2</sub> showed a widened electronic band gap and lower conductivity, which might be due to the weaker orbital interaction between Cu(II) and organic ligand<sup>39, 44, 70</sup> and the relatively larger free void space along the *ab* plane that is not favorable for in-plane charge transport.<sup>54</sup> Another reason for these properties, however, could be the oxidation state of the ligand or the metal within the MOF scaffold, responsible for the negatively charged reduced state of the materials as evidenced by the inferred presence of positively charged NH<sub>4</sub>+ counterions.<sup>71-72</sup>

Inspired by previous reports that the electrical properties of reticular materials composed of redox-active units can be modulated by partial oxidation or reduction through chemical doping,71-73 we further investigated the effect of oxidation on the electrical conductivity of Cu<sub>3</sub>(HHTN)<sub>2</sub> by doping with iodine. A resistor device made by drop-casting the MOF suspension on a gold interdigitated electrode (5 μm gap) was exposed I<sub>2</sub> stream (~ 400 ppm) at room temperature (See section 11 in SI). Exposure of the material to the stream of I2 for about 30 minutes increased the conductance of the device increased significantly by 36000%. The doping process was partially reversible: stopping I2 exposure reversed the current to 157-folds of the original value within 30 mins. XPS characterization showed that I2 doping process likely involved the partial oxidation of both the ligand and metal in the MOF material (Figure S30) and the formation of the I<sub>3</sub><sup>-</sup> ions within the MOFs. PXRD of I2 treated sample exhibited two obvious peaks at  $2\theta$ =3.5° and 7.0°, consistent with the [100] and [200] peaks of pristine Cu<sub>3</sub>(HHTN)<sub>2</sub>, indicating that I<sub>2</sub> doped Cu<sub>3</sub>(HHTN)<sub>2</sub> still maintained the crystalline framework structure. The peak broadening of [100] and [200] diffractions in the I2 treated Cu<sub>3</sub>(HHTN)<sub>2</sub> sample may be due to the possible formation of crystalline I<sub>3</sub>- chains inside the channel that caused the reordering of the MOFs layers. EPR studied showed a new signal with a g value at 1.994 for the iodine-doped Cu<sub>3</sub>(HHTN)<sub>2</sub> sample (Figure S31), indicating the formation of ligand centered radical. Therefore, the increased electrical conductivity of in iodine-doped sample may be due to the improvement in oxidation-induced orbital overlap between the ligand and metal, as well as the formation of free charge carriers through oxidative doping.<sup>72</sup> The increase in conductance upon oxidative doping of Cu<sub>3</sub>(HHTN)<sub>2</sub> MOF suggested a p-type semiconductive character of this material.

#### 3 Conclusions

We have designed and synthesized a new d- $\pi$  conjugated 2D MOF based on the utilization of a new hexatopic ligand HHTN, which is a  $\pi$  extend analog for HHB and HHTP ligands. The reticular incorporation of this large  $\pi$ -conjugated organic building block with Cu ions leads to a Cu<sub>3</sub>(HHTN)<sub>2</sub> MOF with a pore aperture of 2.5 nm, extending the porosity of 2D  $\pi$ -conjugated semiconductive MOF into the mesoporous realm. Cu<sub>3</sub>(HHTN)<sub>2</sub> showed low to moderated electrical conductivity of 9.01×10<sup>-8</sup> S/cm at 385 K and temperature-dependent electrical band gap ranging from 1.65 to 0.75 eV. After chemical oxidation by I<sub>2</sub>, the conductivity of Cu<sub>3</sub>(HHTN)<sub>2</sub> can be improved by 360 times. These results demonstrated the great tunability in conductivity of Cu<sub>3</sub>(HHTN)<sub>2</sub>

using both thermal and chemical stimuli. Despite a computational proposal for achieving a trinaphthylene-based MOF by expanding the size of the ligand,74 the first experimental access and characterization of Cu<sub>3</sub>(HHTN)<sub>2</sub> MOF reported herein constitutes the first experimentally accessible trinaphthylene based d-π conjugated MOF. Thus, our work adds an important member to the previously reported HHB- and HHTP-based MOFs, generating the first isoreticular family of 2D d- $\pi$  conjugated MOFs comprising at least three systematically expanded lattice structures. The lower conductivity and higher porosity found in Cu<sub>3</sub>(HHTN)<sub>2</sub> compared with HHB- and HHTP-based analogs, suggested that porosity and conductivity, which are two important parameters for many electrochemical applications,75 need to be balanced in the design of conductive MOFs. Achieving this delicate balance involves the consideration of several interdependent factors, which can be potentially addressed through a judicious choice of organic ligand and metal node to provide a high-degree orbital overlap of the building blocks, post-synthetic modifications, including doping, redox control, and guest infiltration.71-73, 75-76 We believe these may promote future studies of systematic results structure-property relationships by examining the 2D d-π conjugated MOFs series experimentally to aid the understanding, design, and realization of electrically conductive MOFs, and may offer new opportunities for exploring this class of materials in thermal switching, sensing, and energy-related applications.

#### Acknowledgements

The authors acknowledge support from startup funds provided by Dartmouth College, from the Walter and Constance Burke Research Initiation Award, Irving Institute for Energy and Society, Army Research Office Young Investigator Program Grant No. W911NF-17-1-0398, Sloan Research Fellowship (FG-2018-10561), 3M Non-Tenured Faculty Award, and US Army Cold Regions Research & Engineering Lab (W913E519C0008), National Science Foundation EPSCoR award (#1757371). The authors thank the University Instrumentation Center at the University of New Hampshire (Durham, NH) for the access to XPS.

**Electronic Supplementary Material**: Supplementary material (please give brief details, e.g., further details of the ligand and MOF synthesis and SEM, TEM measurements, XPS, and BET measurements) is available in the online version of this article at http://dx.doi.org/10.1007/s12274-\*\*\*-\*\*\* (automatically inserted by the publisher).

#### References

- [1] Hendon, C. H.; Tiana, D.; Walsh, A. Conductive metal-organic frameworks and networks: Fact or fantasy? *Phys. Chem. Chem. Phys.* **2012**, *14*, 13120-13132.
- [2] Givaja, G.; Amo-Ochoa, P.; Gomez-Garcia, C. J.; Zamora, F. Electrical conductive coordination polymers. *Chem. Soc. Rev.* 2012, 41, 115-147.
- [3] Sun, L.; Campbell, M. G.; Dincă, M. Electrically conductive porous metal-organic frameworks. *Angew. Chem. Int. Ed.* 2016, 55, 3566-3579.
- [4] Ko, M.; Mendecki, L.; Mirica, K. A. Conductive two–dimensional metal-organic frameworks as multifunctional materials. *Chem. Commun.* **2018**, *54*, 7873-7891.

- [5] Huang, X.; Sheng, P.; Tu, Z.; Zhang, F.; Wang, J.; Geng, H.; Zou, Y.; Di, C. A.; Yi, Y.; Sun, Y.; Xu, W.; Zhu, D. A two-dimensional π-d conjugated coordination polymer with extremely high electrical conductivity and ambipolar transport behaviour. *Nat. Commun.* 2015, 6, 7408.
- [6] Dincă, M.; Léonard, F. Metal-organic frameworks for electronics and photonics. MRS Bull. 2016, 41, 854-857.
- [7] Wu, G.; Huang, J.; Zang, Y.; He, J.; Xu, G. Porous field-effect transistors based on a semiconductive metal–organic framework. *J. Am. Chem. Soc.* **2017**, *139*, 1360-1363.
- [8] Campbell, M. G.; Liu, S. F.; Swager, T. M.; Dincă, M. Chemiresistive sensor arrays from conductive 2D metal–organic frameworks. *J. Am. Chem. Soc.* **2015**, *137*, 13780-13783.
- [9] Campbell, M. G.; Sheberla, D.; Liu, S. F.; Swager, T. M.; Dincă, M. Cu<sub>3</sub>(hexaiminotriphenylene)<sub>2</sub>: An electrically conductive 2D metal–organic framework for chemiresistive sensing. *Angew. Chem. Int. Ed.* **2015**, *54*, 4349-4352.
- [10] Smith, M. K.; Jensen, K. E.; Pivak, P. A.; Mirica, K. A. Direct self-assembly of conductive nanorods of metal-organic frameworks into chemiresistive devices on shrinkable polymer films. *Chem. Mater.* **2016**, *28*, 5264-5268.
- [11] Smith, M. K.; Mirica, K. A. Self-organized frameworks on textiles (SOFT): Conductive fabrics for simultaneous sensing, capture, and filtration of gases. J. Am. Chem. Soc. 2017, 139, 16759-16767.
- [12] Campbell, M. G.; Dincă, M. Metal-organic frameworks as active materials in electronic sensor devices. Sensors 2017, 17, 1108.
- [13] Yao, M.-S.; Lv, X.-J.; Fu, Z.-H.; Li, W.-H.; Deng, W.-H.; Wu, G.-D.; Xu, G. Layer-by-layer assembled conductive metal—organic framework nanofilms for room-temperature chemiresistive sensing. *Angew. Chem. Int. Ed.* **2017**, *129*, 16737-16741.
- [14] Mendecki, L.; Mirica, K. A. Conductive metal-organic frameworks as ion-to-electron transducers in potentiometric sensors. ACS Appl. Mater. Interfaces 2018, 10, 19248-19257.
- [15] Rubio-Gimenez, V.; Almora-Barrios, N.; Escorcia-Ariza, G.; Galbiati, M.; Sessolo, M.; Tatay, S.; Marti-Gastaldo, C. Origin of the chemiresistive response of ultrathin films of conductive metal-organic frameworks. *Angew. Chem. Int. Ed.* 2018, 57, 15086-15090.
- [16] Meng, Z.; Aykanat, A.; Mirica, K. A. Welding metallophthalocyanines into bimetallic molecular meshes for ultrasensitive, low-power chemiresistive detection of gases. *J. Am. Chem. Soc.* **2019**, *141*, 2046-2053.
- [17] Aubrey, M. L.; Kapelewski, M. T.; Melville, J. F.; Oktawiec, J.; Presti, D.; Gagliardi, L.; Long, J. R. Chemiresistive detection of gaseous hydrocarbons and interrogation of charge transport in Cu[Ni(2,3-pyrazinedithiolate)<sub>2</sub>] by gas adsorption. *J. Am. Chem. Soc.* **2019**, *141*, 5005-5013.
- [18] Wang, Z.; Liu, T.; Jiang, L.; Asif, M.; Qiu, X.; Yu, Y.; Xiao, F.; Liu, H. Assembling metal—organic frameworks into the fractal scale for sweat sensing. ACS Appl. Mater. Interfaces 2019, 11, 32310-32319.

- [19] Meng, Z.; Stolz, R. M.; Mendecki, L.; Mirica, K. A. Electrically-transduced chemical sensors based on two-dimensional nanomaterials. *Chem. Rev.* **2019**, *119*, 478-598.
- [20] Darago, L. E.; Aubrey, M. L.; Yu, C. J.; Gonzalez, M. I.; Long, J. R. Electronic conductivity, ferrimagnetic ordering, and reductive insertion mediated by organic mixed-valence in a ferric semiquinoid metal-organic framework. *J. Am. Chem. Soc.* **2015**, *137*, 15703-15711.
- [21] DeGayner, J. A.; Jeon, I. R.; Sun, L.; Dincă, M.; Harris, T. D. 2d conductive iron-quinoid magnets ordering up to *Tc* = 105 K via heterogenous redox chemistry. *J. Am. Chem. Soc.* **2017**, *139*, 4175-4184.
- [22] Li, W.; Sun, L.; Qi, J.; Jarillo-Herrero, P.; Dincă, M.; Li, J. High temperature ferromagnetism in π-conjugated two-dimensional metal–organic frameworks. *Chem. Sci.* **2017**, *8*, 2859-2867.
- [23] Dong, R.; Zhang, Z.; Tranca, D. C.; Zhou, S.; Wang, M.; Adler, P.; Liao, Z.; Liu, F.; Sun, Y.; Shi, W.; Zhang, Z.; Zschech, E.; Mannsfeld, S. C. B.; Felser, C.; Feng, X. A coronene-based semiconducting two-dimensional metal–organic framework with ferromagnetic behavior. *Nat. Commun.* **2018**, *9*, 2637.
- [24] Yang, C.; Dong, R.; Wang, M.; Petkov, P. S.; Zhang, Z.; Wang, M.; Han, P.; Ballabio, M.; Brauninger, S. A.; Liao, Z.; Zhang, J.; Schwotzer, F.; Zschech, E.; Klauss, H. H.; Canovas, E.; Kaskel, S.; Bonn, M.; Zhou, S.; Heine, T.; Feng, X. A semiconducting layered metal—organic framework magnet. *Nat. Commun.* **2019**, *10*, 3260.
- [25] Downes, C. A.; Marinescu, S. C. Efficient electrochemical and photoelectrochemical H<sub>2</sub> production from water by a cobalt dithiolene one-dimensional metal–organic surface. *J. Am. Chem. Soc.* **2015**, *137*, 13740-13743.
- [26] Dong, R.; Pfeffermann, M.; Liang, H.; Zheng, Z.; Zhu, X.; Zhang, J.; Feng, X. Large-area, free-standing, two-dimensional supramolecular polymer single-layer sheets for highly efficient electrocatalytic hydrogen evolution. Angew. Chem. Int. Ed. 2015, 54, 12058-12063.
- [27] Miner, E. M.; Fukushima, T.; Sheberla, D.; Sun, L.; Surendranath, Y.; Dincă, M. Electrochemical oxygen reduction catalysed by Ni<sub>3</sub>(hexaiminotriphenylene). *Nat. Commun.* **2016**, *7*, 10942.
- [28] Jia, H.; Yao, Y.; Zhao, J.; Gao, Y.; Luo, Z.; Du, P. A novel two-dimensional nickel phthalocyanine-based metal-organic framework for highly efficient water oxidation catalysis. *J. Mater. Chem. A* **2018**, *6*, 1188-1195.
- [29] Zhong, H.; Ly, K. H.; Wang, M.; Krupskaya, Y.; Han, X.; Zhang, J.; Zhang, J.; Kataev, V.; Buchner, B.; Weidinger, I. M.; Kaskel, S.; Liu, P.; Chen, M.; Dong, R.; Feng, X. A phthalocyanine-based layered two-dimensional conjugated metal–organic framework as a highly efficient electrocatalyst for the oxygen reduction reaction. *Angew. Chem. Int. Ed.* **2019**, *58*, 10677-10682.
- [30] Hu, L.; Xiong, T.; Liu, R.; Hu, Y.; Mao, Y.; Balogun, M. J. T.; Tong, Y. Co<sub>3</sub>O<sub>4</sub>@Cu-based conductive metal–organic framework core-shell nanowire electrocatalysts enable efficient low-overall-potential water splitting. *Chem. Eur. J.* **2019**, *25*, 6575-6583.
- [31] Sheberla, D.; Bachman, J. C.; Elias, J. S.; Sun, C. J.; Shao-Horn, Y.;

Nano Res. 7

Dincă, M. Conductive MOF electrodes for stable supercapacitors with high areal capacitance. *Nat. Mater.* **2016**, *16*, 220-225.

- [32] Zhang, Z.; Awaga, K. Redox-active metal-organic frameworks as electrode materials for batteries. *MRS Bull.* **2016**, *41*, 883-889.
- [33] Park, J.; Lee, M.; Feng, D.; Huang, Z.; Hinckley, A. C.; Yakovenko, A.; Zou, X.; Cui, Y.; Bao, Z. Stabilization of hexaaminobenzene in a 2D conductive metal–organic framework for high power sodium storage. *J. Am. Chem. Soc.* **2018**, *140*, 10315-10323.
- [34] Feng, D.; Lei, T.; Lukatskaya, M. R.; Park, J.; Huang, Z.; Lee, M.; Shaw, L.; Chen, S.; Yakovenko, A. A.; Kulkarni, A.; Xiao, J.; Fredrickson, K.; Tok, J. B.; Zou, X.; Cui, Y.; Bao, Z. Robust and conductive two-dimensional metal—organic frameworks with exceptionally high volumetric and areal capacitance. *Nat. Energy* **2018**, *3*, 30-36.
- [35] Zhou, S.; Kong, X.; Zheng, B.; Huo, F.; Stromme, M.; Xu, C. Cellulose nanofiber@conductive metal—organic frameworks for high-performance flexible supercapacitors. *ACS Nano* **2019**, *13*, 9578-9586.
- [36] Zhang, X.; Dong, P.; Song, M. K. Metal-organic frameworks for high-energy lithium batteries with enhanced safety: Recent progress and future perspectives. *Batteries Supercaps* **2019**, *2*, 591-626.
- [37] Nam, K. W.; Park, S. S.; Dos Reis, R.; Dravid, V. P.; Kim, H.; Mirkin, C. A.; Stoddart, J. F. Conductive 2D metal–organic framework for high-performance cathodes in aqueous rechargeable zinc batteries. *Nat. Commun.* **2019**, *10*, 4948.
- [38] Hmadeh, M.; Lu, Z.; Liu, Z.; Gándara, F.; Furukawa, H.; Wan, S.; Augustyn, V.; Chang, R.; Liao, L.; Zhou, F.; Perre, E.; Ozolins, V.; Suenaga, K.; Duan, X.; Dunn, B.; Yamamto, Y.; Terasaki, O.; Yaghi, O. M. New porous crystals of extended metal-catecholates. *Chem. Mater.* **2012**, *24*, 3511-3513.
- [39] Leong, C. F.; Usov, P. M.; D'Alessandro, D. M. Intrinsically conducting metal-organic frameworks. MRS Bull. 2016, 41, 858-864.
- [40] Nagatomi, H.; Yanai, N.; Yamada, T.; Shiraishi, K.; Kimizuka, N. Synthesis and electric properties of a two-dimensional metal–organic framework based on phthalocyanine. *Chem. Eur. J.* **2018**, *24*, 1806-1810.
- [41] Kambe, T.; Sakamoto, R.; Hoshiko, K.; Takada, K.; Miyachi, M.; Ryu, J. H.; Sasaki, S.; Kim, J.; Nakazato, K.; Takata, M.; Nishihara, H. π-conjugated nickel bis(dithiolene) complex nanosheet. *J. Am. Chem. Soc.* **2013**, *135*, 2462-2465.
- [42] Clough, A. J.; Yoo, J. W.; Mecklenburg, M. H.; Marinescu, S. C. Two-dimensional metal–organic surfaces for efficient hydrogen evolution from water. *J. Am. Chem. Soc.* **2015**, *137*, 118-121.
- [43] Dou, J. H.; Sun, L.; Ge, Y.; Li, W.; Hendon, C. H.; Li, J.; Gul, S.; Yano, J.; Stach, E. A.; Dincă, M. Signature of metallic behavior in the metal–organic frameworks M<sub>3</sub>(hexaiminobenzene)<sub>2</sub> (M = Ni, Cu). *J. Am. Chem. Soc.* **2017**, 139, 13608–13611.
- [44] Park, J.; Hinckley, A. C.; Huang, Z.; Feng, D.; Yakovenko, A. A.; Lee, M.; Chen, S.; Zou, X.; Bao, Z. Synthetic routes for a 2D semiconductive copper hexahydroxybenzene metal–organic framework. *J. Am. Chem. Soc.* **2018**, *140*,

14533-14537.

- [45] Sheberla, D.; Sun, L.; Blood-Forsythe, M. A.; Er, S.; Wade, C. R.; Brozek, C. K.; Aspuru-Guzik, A.; Dincă, M. High electrical conductivity in Ni<sub>3</sub>(2,3,6,7,10,11-hexaiminotriphenylene)<sub>2</sub>, a semiconducting metal–organic graphene analogue. *J. Am. Chem. Soc.* **2014**, *136*, 8859-8862.
- [46] Clough, A. J.; Skelton, J. M.; Downes, C. A.; de la Rosa, A. A.; Yoo, J. W.; Walsh, A.; Melot, B. C.; Marinescu, S. C. Metallic conductivity in a two-dimensional cobalt dithiolene metal—organic framework. *J. Am. Chem. Soc.* 2017, *139*, 10863-10867.
- [47] Rubio-Gimenez, V.; Galbiati, M.; Castells-Gil, J.; Almora-Barrios, N.; Navarro-Sanchez, J.; Escorcia-Ariza, G.; Mattera, M.; Arnold, T.; Rawle, J.; Tatay, S.; Coronado, E.; Marti-Gastaldo, C. Bottom-up fabrication of semiconductive metal—organic framework ultrathin films. *Adv. Mater.* **2018**, 30, 1704291.
- [48] Cui, Y.; Yan, J.; Chen, Z.; Zhang, J.; Zou, Y.; Sun, Y.; Xu, W.; Zhu, D.  $[Cu_3(C_6Se_6)]_n$ : The first highly conductive 2D  $\pi$ -d conjugated coordination polymer based on benzenehexaselenolate. *Adv. Sci.* **2019**, *6*, 1802235.
- [49] Cui, Y.; Yan, J.; Chen, Z.; Xing, W.; Ye, C.; Li, X.; Zou, Y.; Sun, Y.; Liu, C.; Xu, W.; Zhu, D. Synthetic route to a triphenylenehexaselenol-based metal organic framework with semi-conductive and glassy magnetic properties. iScience 2020, 23, 100812.
- [50] Eddaoudi, M.; Kim, J.; Rosi, N.; Vodak, D.; Wachter, J.; O'Keeffe, M.; Yaghi, O. M. Systematic design of pore size and functionality in isoreticular MOFs and their application in methane storage. *Science* **2002**, *295*, 469-472.
- [51] Furukawa, H.; Ko, N.; Go, Y. B.; Aratani, N.; Choi, S. B.; Choi, E.; Yazaydin, A. O.; Snurr, R. Q.; O'Keeffe, M.; Kim, J.; Yaghi, O. M. Ultrahigh porosity in metal–organic frameworks. *Science* **2010**, *329*, 424-428.
- [52] Furukawa, H.; Go, Y. B.; Ko, N.; Park, Y. K.; Uribe-Romo, F. J.; Kim, J.; O'Keeffe, M.; Yaghi, O. M. Isoreticular expansion of metal—organic frameworks with triangular and square building units and the lowest calculated density for porous crystals. *Inorg. Chem.* **2011**, *50*, 9147-9152.
- [53] Deng, H.; Grunder, S.; Cordova, K. E.; Valente, C.; Furukawa, H.; Hmadeh, M.; Gandara, F.; Whalley, A. C.; Liu, Z.; Asahina, S.; Kazumori, H.; O'Keeffe, M.; Terasaki, O.; Stoddart, J. F.; Yaghi, O. M. Large-pore apertures in a series of metal–organic frameworks. *Science* **2012**, *336*, 1018-1023.
- [54] Walsh, A.; Butler, K. T.; Hendon, C. H. Chemical principles for electroactive metal-organic frameworks. MRS Bull. 2016, 41, 870-876.
- [55] Rudiger, E. C.; Rominger, F.; Steuer, L.; Bunz, U. H. Synthesis of substituted trinaphthylenes. J. Org. Chem. 2016, 81, 193-196.
- [56] Li, W.-H.; Ding, K.; Tian, H.-R.; Yao, M.-S.; Nath, B.; Deng, W.-H.; Wang, Y.; Xu, G. Conductive metal-organic framework nanowire array electrodes for high-performance solid-state supercapacitors. *Adv. Funct. Mater.* 2017, 27, 1702067.
- [57] Chen, S.; Dai, J.; Zeng, X. C. Metal-organic kagome lattices  $M_3(2,3,6,7,10,11$ -hexaiminotriphenylene)<sub>2</sub> (M = Ni and Cu): From semiconducting to metallic by metal substitution. *Phys. Chem. Chem. Phys.*

Nano Res.

2015, 17, 5954-5958.

- [58] Ko, M.; Aykanat, A.; Smith, M. K.; Mirica, K. A. Drawing sensors with ball-milled blends of metal–organic frameworks and graphite. *Sensors* **2017**, *17*, 2192.
- [59] Fan, H. Y. Temperature dependence of the energy gap in semiconductors. *Phys. Rev.* **1951**, *82*, 900-905.
- [60] Varshni, Y. P. Temperature dependence of the energy gap in semiconductors. *Physica* **1967**, *34*, 149-154.
- [61] Bludau, W.; Onton, A.; Heinke, W. Temperature dependence of the band gap of silicon. *J. Appl. Phys.* **1974**, *45*, 1846-1848.
- [62] Ünlü, H. A thermodynamic model for determining pressure and temperature effects on the bandgap energies and other properties of some semiconductors. *Solid State Electron.* **1992**, *35*, 1343-1352.
- [63] Geng, P. J.; Li, W. G.; Zhang, X. H.; Zhang, X. Y.; Deng, Y.; Kou, H. B. A novel theoretical model for the temperature dependence of band gap energy in semiconductors. *J. Phys. D: Appl. Phys.* **2017**, *50*, 40LT02.
- [64] Birkett, M.; Linhart, W. M.; Stoner, J.; Phillips, L. J.; Durose, K.; Alaria, J.; Major, J. D.; Kudrawiec, R.; Veal, T. D. Band gap temperature-dependence of close-space sublimation grown Sb<sub>2</sub>Se<sub>3</sub> by photo-reflectance. *APL Mater.* **2018**, *6*, 084901.
- [65] Chirvase, D.; Chiguvare, Z.; Knipper, M.; Parisi, J.; Dyakonov, V.; Hummelen, J. C. Temperature dependent characteristics of poly(3 hexylthiophene)-fullerene based heterojunction organic solar cells. *J. Appl. Phys.* **2003**, *93*, 3376-3383.
- [66] Mirsakiyeva, A.; Hugosson, H. W.; Linares, M.; Delin, A. Temperature dependence of band gaps and conformational disorder in pedot and its selenium and tellurium derivatives: Density functional calculations. *J. Chem. Phys.* **2017**, *147*, 134906.
- [67] Wang, S.; Ma, J.; Li, W.; Wang, J.; Wang, H.; Shen, H.; Li, J.; Wang, J.; Luo, H.; Li, D. Temperature-dependent band gap in two-dimensional perovskites: Thermal expansion interaction and electron-phonon interaction. *J. Phys. Chem. Lett.* **2019**, *10*, 2546-2553.
- [68] Tyagi, P.; Vedeshwar, A. G. Grain size dependent optical band gap of

- cdi2 films. Bull. Mater. Sci. 2001, 24, 297-300.
- [69] Pejova, B.; Grozdanov, I.; Tanuševski, A. Optical and thermal band gap energy of chemically deposited bismuth(III) selenide thin films. *Mater. Chem. Phys.* **2004**, 83, 245-249.
- [70] Tiana, D.; Hendon, C. H.; Walsh, A.; Vaid, T. P. Computational screening of structural and compositional factors for electrically conductive coordination polymers. *Phys. Chem. Chem. Phys.* 2014, 16, 14463-14472.
- [71] Kambe, T.; Sakamoto, R.; Kusamoto, T.; Pal, T.; Fukui, N.; Hoshiko, K.; Shimojima, T.; Wang, Z.; Hirahara, T.; Ishizaka, K.; Hasegawa, S.; Liu, F.; Nishihara, H. Redox control and high conductivity of nickel bis(dithiolene) complex π-nanosheet: a potential organic two-dimensional topological insulator. *J. Am. Chem. Soc.* **2014**, *136*, 14357-14360.
- [72] Jiang, Y.; Oh, I.; Joo, S. H.; Buyukcakir, O.; Chen, X.; Lee, S. H.; Huang, M.; Seong, W. K.; Kwak, S. K.; Yoo, J. W.; Ruoff, R. S. Partial oxidation-induced electrical conductivity and paramagnetism in a Ni(II) tetraaza[14]annulene-linked metal organic framework. *J. Am. Chem. Soc.* **2019**, *141*, 16884-16893.
- [73] Aubrey, M. L.; Wiers, B. M.; Andrews, S. C.; Sakurai, T.; Reyes-Lillo, S. E.; Hamed, S. M.; Yu, C. J.; Darago, L. E.; Mason, J. A.; Baeg, J. O.; Grandjean, F.; Long, G. J.; Seki, S.; Neaton, J. B.; Yang, P.; Long, J. R. Electron delocalization and charge mobility as a function of reduction in a metal-organic framework. *Nat. Mater.* **2018**, *17*, 625-632.
- [74] Bi, S.; Banda, H.; Chen, M.; Niu, L.; Chen, M.; Wu, T.; Wang, J.; Wang, R.; Feng, J.; Chen, T.; Dincă, M.; Kornyshev, A. A.; Feng, G. Molecular understanding of charge storage and charging dynamics in supercapacitors with MOF electrodes and ionic liquid electrolytes. *Nat. Mater.* **2020.** DOI: https://doi.org/10.1038/s41563-019-0598-7.
- [75] Zhang, Y.; Riduan, S. N.; Wang, J. Redox active metal- and covalent organic frameworks for energy storage: balancing porosity and electrical conductivity. *Chem. Eur. J.* **2017**, *23*, 16419-16431.
- [76] Li, P.; Wang, B. Recent development and application of conductive MOFs. Isr. J. Chem. 2018, 58, 1010-1018.

## **Electronic Supplementary Material**

## Two-dimensional d-π conjugated metal-organic framework based on hexahydroxytrinaphthylene

Zheng Meng<sup>1</sup> and Katherine A. Mirica<sup>1</sup>( )

Department of Chemistry, Burke Laboratory, 41 College Street, Dartmouth College, Hanover, NH 03755, United States

Supporting information to DOI 10.1007/s12274-\*\*\*\*-\* (automatically inserted by the publisher)

#### Content

ι.	Materials and Methods		
2.	Synthesis	S97	
2	2.1. Synthesis of HHTN Ligand	S97	
2	2.2. Synthesis of Cu <sub>3</sub> (HHTN) <sub>2</sub> MOF	S101	
3.	FTIR Spectrum	S103	
1.	X-ray Photoelectron Spectroscopy	S104	
5.	Structure Analysis by Computational Study and Powder X-ray Diffraction	S105	
<b>5.</b>	SEM and TEM	S109	
7.	Electron Paramagnetic Spectroscopy (EPR)	S110	
3.	Thermal Gravimetric Analyses (TGA)	S111	
).	Brunauer-Emmett-Teller (BET) Analysis	S112	
١٥.	Measurement of Conductivity	S113	
11.	I <sub>2</sub> Doping Study of Cu <sub>3</sub> (HHTN) <sub>2</sub>	S115	
Dof	ionom cos	C110	

Address correspondence to First A. Firstauthor, email1; Third C. Thirdauthor, email2

#### 1. Materials and Methods

2,3-Dihydroxynaphthalene (CAS N.O.: 92-44-4), glacial acetic acid (CAS N.O.: 64-19-7), liquid bromine (CAS N.O.: 24959-67-9), tin(II) chloride dihydrate (CAS N.O.: 10025-69-1), iodomethane (CAS N.O.: 74-88-4), 2,2'-bipyridine (CAS N.O.: 366-18-7), THF (CAS N.O.: 109-99-9), Ni(1,5-COD)<sub>2</sub> (CAS N.O.: 1295-35-8), boron bromide (CAS N.O.: 10294-33-4), ammonia water (28%-30%, CAS N.O.: 1336-21-6) were purchased from Sigma Aldrich. Hexane (CAS N.O.: 110-54-3), acetonitrile (CAS N.O.: 75-05-8), DMSO (CAS N.O.: 67-68-5), concentrated HCl (37%, CAS N.O.: 7647-01-0) were purchased from BDH Chemicals. 1,5-Cyclooctadiene (CAS N.O.: 111-78-4) and K<sub>2</sub>CO<sub>3</sub> (CAS N.O.: 584-08-7) were purchased from Alfa Aesar. Melting points were determined using a Focus X-4 apparatus, and were not corrected. Analytical thin-layer chromatography (TLC) was performed on Merck silica gel 60 F254 plates. Compounds 6,7-dibromonaphthalene-2,3-diol 3,¹ 2,3-dibromo-6,7-dimethoxynaphthalene 4² were synthesized according to the literature procedures. The synthesis of 2,3,8,9,14,15-hexamethoxytrinaphthylene (HMTN) was referenced form the procedure reported by Bunz's group with an optimized work-up process. The yields were given as isolated yields. NMR spectra were recorded on a Bruker 600 MHz NMR spectrometer. The chemical shifts (δ) were expressed in ppm with internal standard tetramethylsilane (TMS) and solvent signals as internal references, and J values were given in Hz. Standard abbreviations indicating multiplicity were used as follows: s (singlet), br (broad), d (doublet), t (triplet), q (quartet), m (multiple).

Scanning Electron Microscopy (SEM) and Energy Dispersive X-ray Spectroscopy (EDX) were performed using a Hitachi TM3000 SEM (Tokyo, Japan) equipped for X-ray microanalysis with a Bruker Edax light element Si(Li) detector (Billerica, MA). Transmission electron microscopy was carried out at a Tecnai F20ST FEG TEM instrument. Powder X-ray diffraction (PXRD) measurements were performed with a Bruker D8 diffractometer equipped with a Ge-monochromated 2.2 kW (40 kV, 40 mA) CuKα (λ= 1.54 Å) radiation source and a NaI scintillation counter detector (Billerica, MA). EmStat MUX16 potentiostat (Palm Instruments BV, Netherlands) was used for electrochemical measurements. Nitrogen adsorption experiments were performed with an Micrometrics 3Flex Porosity Analyzer (Norcross GA).

#### 2. Synthesis

#### 2.1. Synthesis of HHTN Ligand

**Scheme S1**. The synthesis of hexamethoxytrinaphthylene HMTN.

Synthesis of 1,4,6,7-tetrabromonaphthalene-2,3-diol 2. 2,3-Dihydroxynaphthalene (9.0 g, 56 mmol) was dissolved in 90 mL of glacial acetic acid, and then liquid bromine (12.8 mL, 0.25 mmol) was slowly added in 40 minutes during which the reaction was violently stirred. The stirred solution was then heated at reflux for 1 hour. Then the reaction mixture was cooled ca. 50 °C. And the resulting precipitate was collected by suction filtration and washed with 50 mL of hexane, which gives 2 as a white solid after being dried (25.2 g, 94%). The compound is pure enough for the characterization and was used directly for the next step. <sup>1</sup>H NMR (600 MHz, CDCl<sub>3</sub>)  $\delta$  = 8.34 (s, 1H), 6.21 (s, 1H); <sup>13</sup>C NMR (150 MHz, DMSO-d<sub>6</sub>)  $\delta$  = 147.04, 130.28, 127.80, 121.09, 104.51; HRMS (EI): m/z calcd for C<sub>10</sub>H<sub>4</sub>Br<sub>4</sub>O<sub>2</sub>: 471.6945; found: 471.6955 [M]<sup>+</sup>.

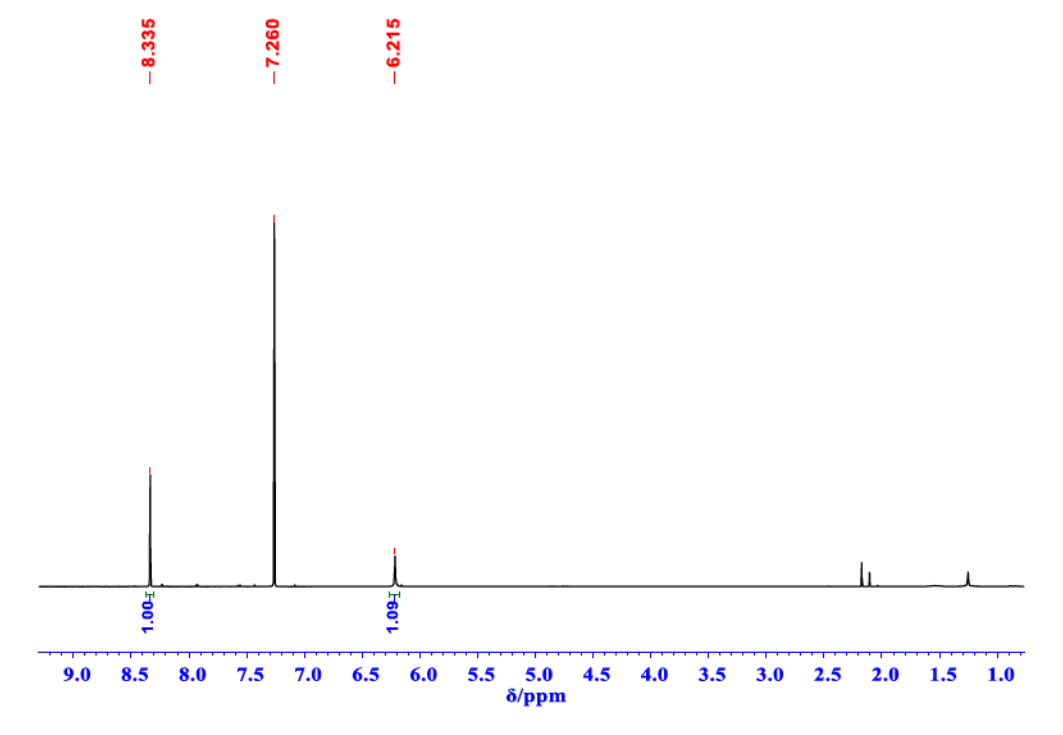


Figure S1. <sup>1</sup>H NMR spectrum (CDCl<sub>3</sub>, 600 MHz, 298 K) of 2.

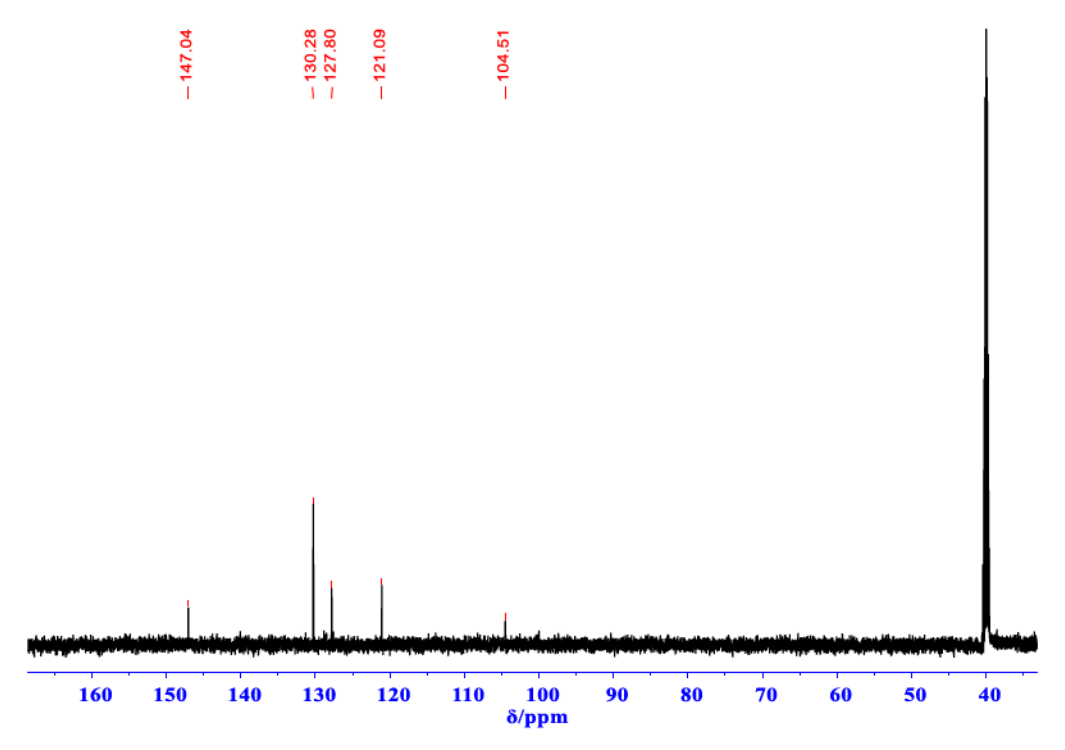


Figure S2. <sup>13</sup>C NMR spectrum (DMSO-d<sub>6</sub>, 150 MHz, 298 K) of 2.

Synthesis of 6,7-dibromonaphthalene-2,3-diol 3. Compound 3 was synthesized by following a previously reported procedure. Compound 2 (20 g, 42 mmol) was then dissolved in 350 mL of glacial acetic acid and tin(II) chloride dihydrate (80 g) was added. The mixture was heated near reflux and concentrated HCl (120 mL) was added which result in the evolution of a large amount of HBr gas. The mixture was heated at reflux for 50 minutes, the solution was then cooled to room temperature and poured into 500 mL of aqueous HCl solution. A white precipitate was formed which was then filtrated after the mixture was stood overnight. The product was obtained as a white powder (10.3 g, 77%). The characterization data (<sup>1</sup>H and <sup>13</sup>C NMR) was the same as reported in the literature.<sup>1</sup>

Synthesis of 2,3-Dibromo-6,7-dimethoxynaphthalene 4. Compound 3 (8 g, 31.4 mmol) was dissolved in acetonitrile (50 mL), then K<sub>2</sub>CO<sub>3</sub> (10.9g, 78.5 mmol, 2.5 equivalents) and iodomethane (4.9 mL,78.5 mmol, 2.5 equivalents) were successively added. The flask was then sealed and the reaction mixture was heated under 75 °C for 18 hours. The reaction mixture was then cooled down room temperature and diluted with 300 mL of CH<sub>2</sub>Cl<sub>2</sub>, then washed with water (200 mL × 3). The organic phase was dried under vacuum to give a compound 4 as white solid (10 g, 92%), whose characterization data (<sup>1</sup>H and <sup>13</sup>C NMR) is in consistence with the literature report.<sup>2</sup>

Synthesis of 2,3,8,9,14,15,20,21-octamethoxytetranaphthylene (HMTN). Under Ar atmosphere, 1.5 mL (12 mmol, 2 equivalents) of 1,5-cyclooctadiene and 1.17 g (7.5 mmol, 1.25 equiv) of 2,2'-bipyridine were added to a Schlenk flask charged with 50 mL dry THF. Then 2.1 g of Ni(1,5-COD)<sub>2</sub> (7.5 mmol, 1.25 equiv) was added which gave a purple solution. A THF solution of dibromonaphthalene 4 (2.07 g, 6 mmol in 25 mL) was added dropwise over 30 min. A gray mixture was formed after 2 hours. After the mixture was stirred at ambient temperature for another 18 h, the solvent was evaporated under vacuum. Then 250 mL of dichloromethane was added to the residue and the suspension was sonicated and then filtrated. The filter cake was washed with dichloromethane (25 mL × 3). The organic filtrate was washed with water for three times (300 mL × 3). The organic phase was further condensed to approximately 80 mL, which was then placed

into a refrigerator set at -10 °C. The triply coupling product HMTN could be obtained as a colorless crystalline solid after filtration (470 mg, 42%), which gives the same characterization date as the literature report.

The mother liquid was collected and subjected to column chromatography (eluent CH<sub>2</sub>Cl<sub>2</sub>→EtOAc: hexane=1: 4). 468 mg of a mixture of HMTN and the quadruple coupling product OMTN as cyclooctatetraene derivative (structure shown in **Scheme S1**) could be obtained and identified by <sup>1</sup>H NMR and MALDI-TOF spectrum.

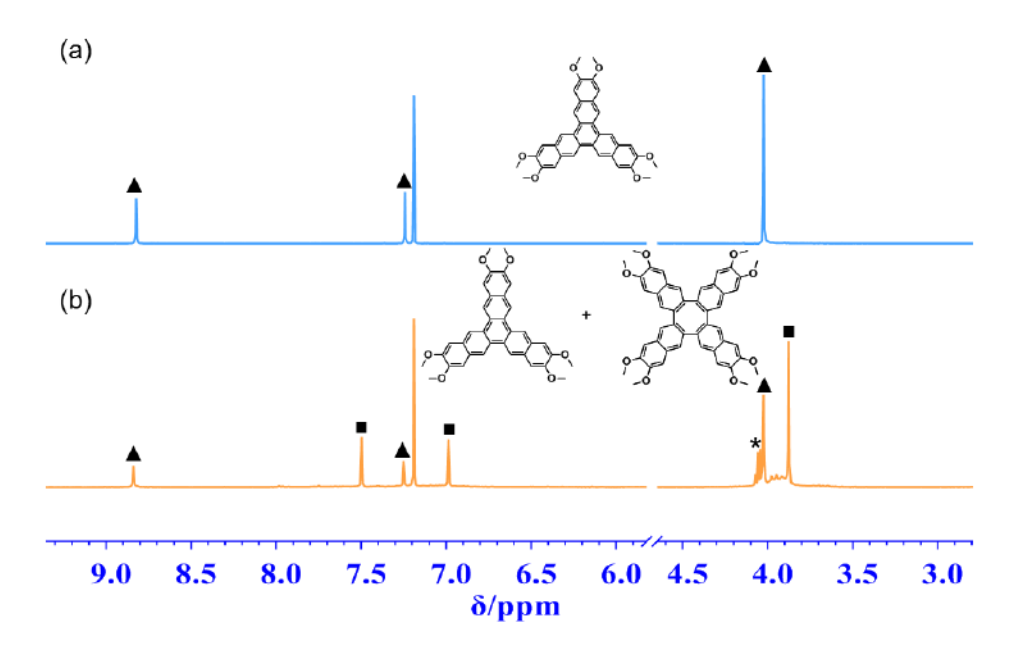


**Figure S3.** ¹H NMR spectrum (CDCl<sub>3</sub>, 600 MHz, 298 K) of ligand HHTM (a) and a mixture of HMTN (peaks marked with ▲) and the quadruple coupling product OMTN (peaks marked with •). The peaks marked with \* are from ethyl acetate.

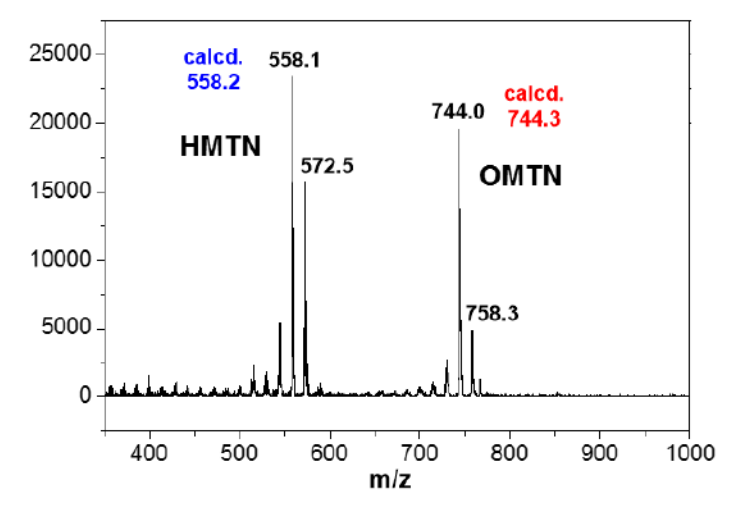


Figure S4. MALDI-TOF mass spectrum of a mixture of HMTN and the quadruple coupling product OMTN.

**Scheme S2**. The synthesis of HHTN.

Synthesis of 2,3,8,9,14,15-hexahydroxytrinaphthylene (HHTN). To a solution of HMTN (400 mg, 0.72 mmol) in dry dichloromethane (30 mL) in an ice bath was added boron bromide (1.3 mL, 13 mmol, 18 equivalents). After being stirred at r.t. for 24 h, the reaction mixture was poured into ice water (100 mL) and stirred for another 30 min, then filtrated, washed with water and dried under vacuum to give 304 mg (89 %) of HHTN as a gray solid. M.p.: >300 °C; <sup>1</sup>H NMR (600 MHz, DMSO- $d_6$ )  $\delta$  = 9.71 (s, 6H), 8.90 (s, 6H), 7.34 (s, 6H); <sup>13</sup>C NMR (150 MHz, DMSO- $d_6$ )  $\delta$  = 148.0, 129.0, 126.6, 120.0, 109.5; HRMS (ESI): m/z calcd for C<sub>30</sub>H<sub>19</sub>O<sub>6</sub>: 475.1176; found: 475.1180 [M+H]<sup>+</sup>.

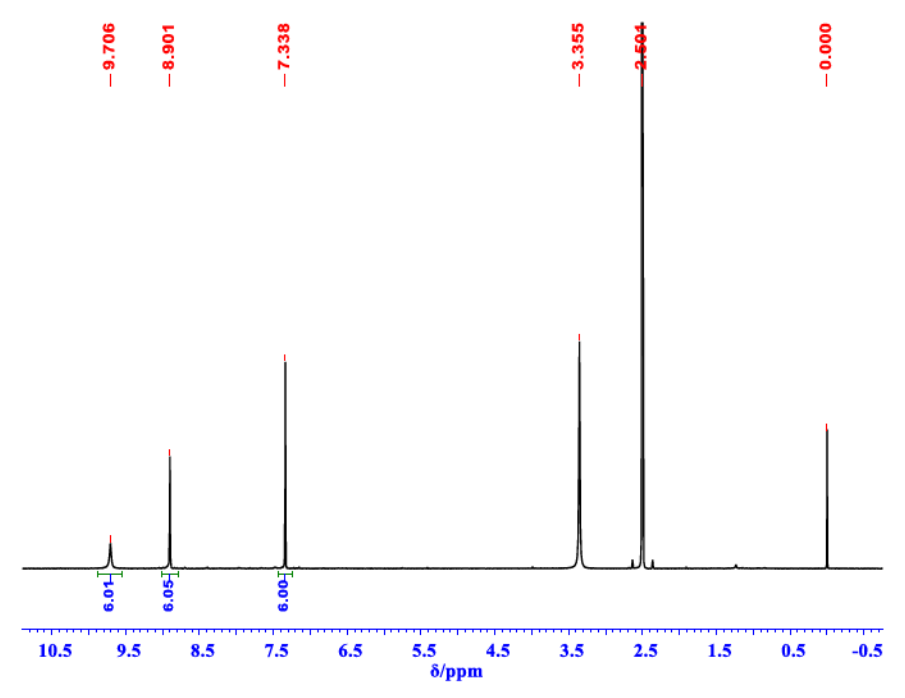


Figure S5. <sup>1</sup>H NMR spectrum (DMSO, 600 MHz, 298 K) of ligand HHTN.



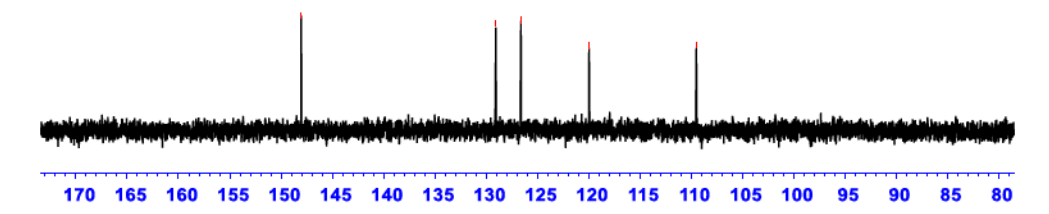


Figure S6. <sup>13</sup>C NMR spectrum (DMSO, 150 MHz, 298 K) of ligand HHTN.

#### 2.2. Synthesis of Cu<sub>3</sub>(HHTN)<sub>2</sub> MOF

Different conditions, including the variation of the solvent system, concentration of ligand, and the use of base have been tried for the synthesis of Cu<sub>3</sub>(HHTN)<sub>2</sub> MOF (**Table S1**). It is found that the addition of base (ammonia water (25 wt%) or ethylenediamine) is necessary for the deprotonation of the catechol to facilitate the coordination, because the in pure solvents, such as DMSO and DMI, no solid product was formed without the addition of the base. DMI/H<sub>2</sub>O (v/v=3:1) was found the optimal solvent among the solvent systems tested which has a moderate solubility for the ligand and produced the crystalline MOF materials. Our effort generated multiple conditions for obtaining highly crystalline material of Cu<sub>3</sub>(HHTN)<sub>2</sub> (**Table S1**), including **entry 7**, **9**, **14**, **15** and **16**, in which the condition in **entry 9** was identified as the optimal, considering the intensity, relative ratio, and full width at half maximum of the PXRD peaks (**Figure S7**), as well as the morphology of the samples obtained (see **Figure S21** in **section 7**).

Optimized condition: To a 20 mL vial charged with 54.5 mg of copper(II) acetate (0.30 mmol, 2 eq. to HHTN) and 15 mL DMI/H<sub>2</sub>O (v/v=3:1), 1.50 mL concentrated ammonia water (25%~28%, 150 eq to HHTN) was added. A clear and dark blue solution was formed after gently shaking the vial for 0.5 to 1 min. To this solution, 71 mg of HHTN (0.15 mmol) was added. The mixture was sonicated for 1 minute to get a homogeneous yellowish suspension, which was then transferred on to hotplate and heated at 65 °C with the vial loosely capped under air. After 24 hours, the reaction was filtrated, and the solid was washed with water (5 × 20 mL) and acetone (5 × 20 mL). The solid was then dried using an oil pump under room temperature for 1 day to afford a dark brown powder (75 mg, yield 87% based on the formula Cu<sub>3</sub>(HHTN)<sub>2</sub>). This as-synthesized material was used for PXRD, FTIR, XPS, UV-vis-NIR, and elemental analysis.

Table S1. The trial of different synthetic conditions for Cu<sub>3</sub>(HHTN)<sub>2</sub>.

N.O.	Solvent	[L]/(mM)	Base or Additives	Time (h)/Temp.
1	DMSO	30	NH <sub>3</sub> •H <sub>2</sub> O (50 eq)	24/85 °C, N <sub>2</sub>
2	DMSO	30	NH <sub>3</sub> •H <sub>2</sub> O (50 eq)	72/150 °C
3	$H_2O$	30	NH <sub>4</sub> OAc	24/85 °C
4	DMSO:H <sub>2</sub> O=1:1	30	NH <sub>3</sub> •H <sub>2</sub> O (50 eq)	24/85 °C
5	benzene:DMSO=1:1	30	NH <sub>3</sub> •H <sub>2</sub> O (50 eq)	24/85 °C
6	DMSO	30	en (50 eq)	24/65 °C
7	H <sub>2</sub> O:DMI=1:3	30	NH <sub>3</sub> •H <sub>2</sub> O (50 eq)	24/65 °C
8	H <sub>2</sub> O:DMI=1:3	30	en (50 eq)	24/65 °C
9	H <sub>2</sub> O:DMI=1:3	10	NH <sub>3</sub> •H <sub>2</sub> O (150 eq)	24/65 °C
10	H <sub>2</sub> O:DMI=1:3	30	NH <sub>3</sub> •H <sub>2</sub> O (50 eq)	24/85 °C
11	H <sub>2</sub> O:DMI=1:3	10	NH <sub>3</sub> •H <sub>2</sub> O (50 eq)	48/65 °C
12	H <sub>2</sub> O:DMI=1:3	10	NH <sub>3</sub> •H <sub>2</sub> O (150 eq)	48/65 °C
13	H <sub>2</sub> O:DMI=1:3	10	NH <sub>3</sub> •H <sub>2</sub> O (300 eq)	24/65 °C
14	H <sub>2</sub> O:NMP=1:3	10	NH <sub>3</sub> •H <sub>2</sub> O (300 eq)	24/65 °C
15	H <sub>2</sub> O:DMI=1:3	10	en (50 eq), $Cu(NO_3)_2$	24/65 °C
16	H <sub>2</sub> O:DMI=1:3	5	en (50 eq), $Cu(NO_3)_2$	24/65 °C

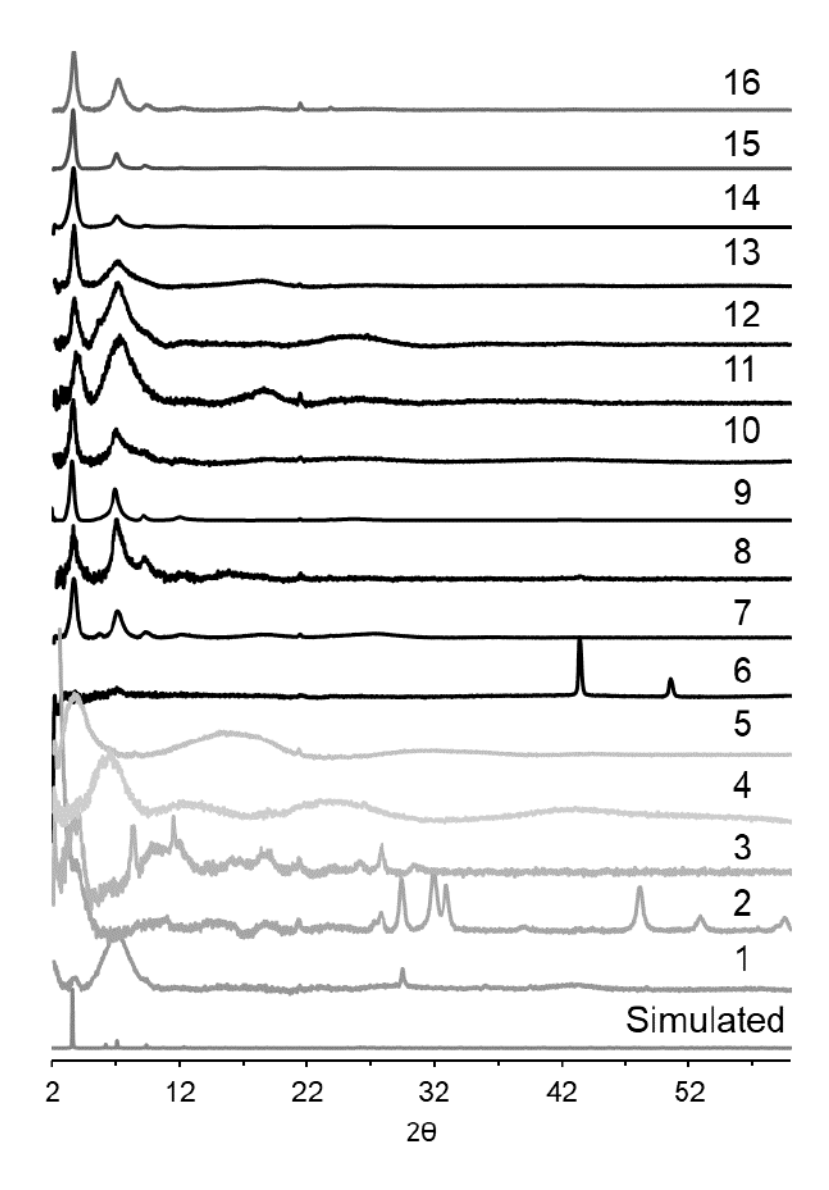


Figure S7. PXRD of the materials obtained under synthetic conditions demonstrated in Table S1 and simulated PXRD of Cu<sub>3</sub>(HHTN)<sub>2</sub>.

#### 3. FTIR Spectrum

Infrared spectra were recorded on a JASCO model FT IR-6100 Fourier transform infrared spectrophotometer. The material was mixed with KBr powder in a mass ratio of ~1:50 and then pressed into a pellet in a die with a diameter of 8 mm under nonspecific pressures. HHTN was directly used after it was isolated as described in **section 2.1**. Cu<sub>3</sub>(HHTN)<sub>2</sub> was used after it was further dried in a vacuum desiccator equipped with an oil pump for 24 hours under room temperature after synthesis.

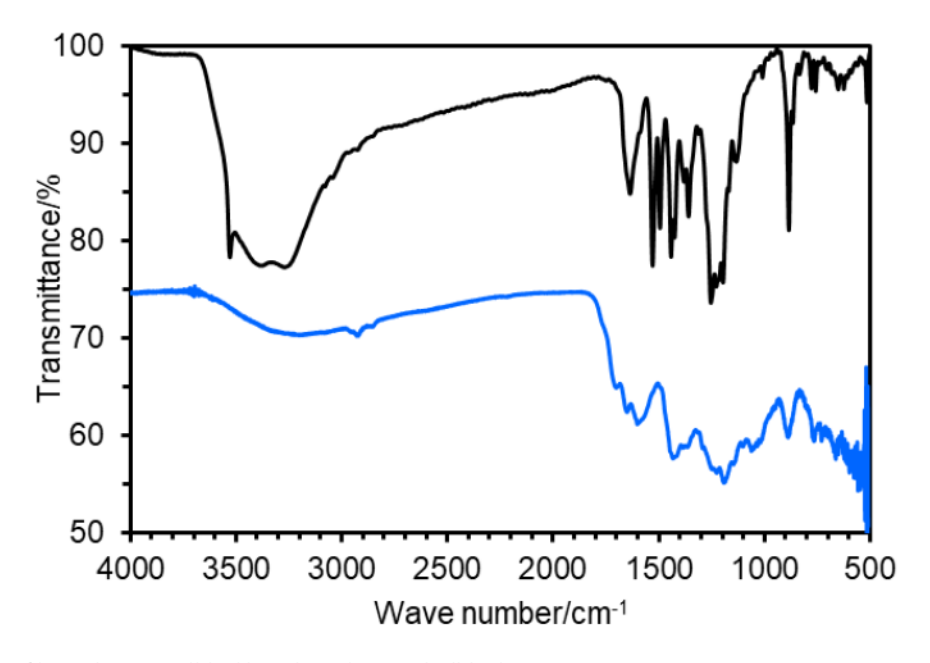


Figure S8. FTIR spectra of ligand HHTN (black) and Cu<sub>3</sub>(HHTN)<sub>2</sub> (blue).

#### 4. X-ray Photoelectron Spectroscopy

X-ray photoelectron spectroscopy (XPS) experiments were conducted on a Kratos Analytical AXIS Supra X-ray Photoelectron Spectrometer under ultrahigh vacuum (base pressure  $10^{-7}$  Torr). The measurement chamber was equipped with a monochromatic Al (K $\alpha$ ) X-ray source. The material was mounted by pressing it onto copper tape which was mounted on a Dual-Height (Kratos) sample holder. The survey spectrum was obtained from 0 eV–1200 eV to obtain elemental surface composition. High-resolution spectra (C 1s, N 1s, O 1s, Cu 2p3/2, I3d) were then performed at energy regions specific to elements observed in the survey spectrum. Both survey and high-resolution spectra were obtained using a beam diameter of 200  $\mu$ m.

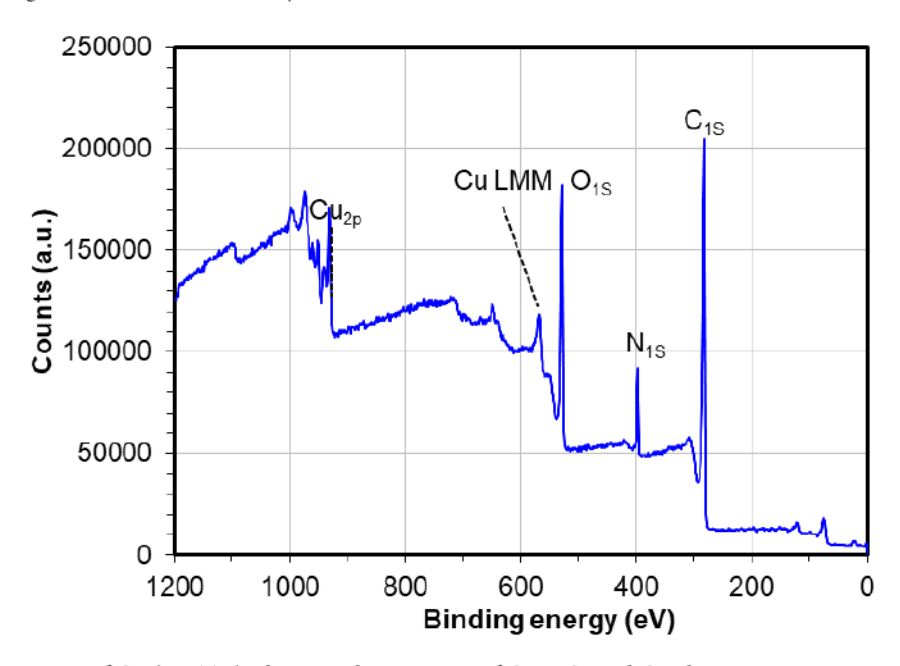


Figure S9. XPS survey spectrum of Cu<sub>3</sub>(HHTN)<sub>2</sub> showing the presence of C, N, O, and Cu elements.

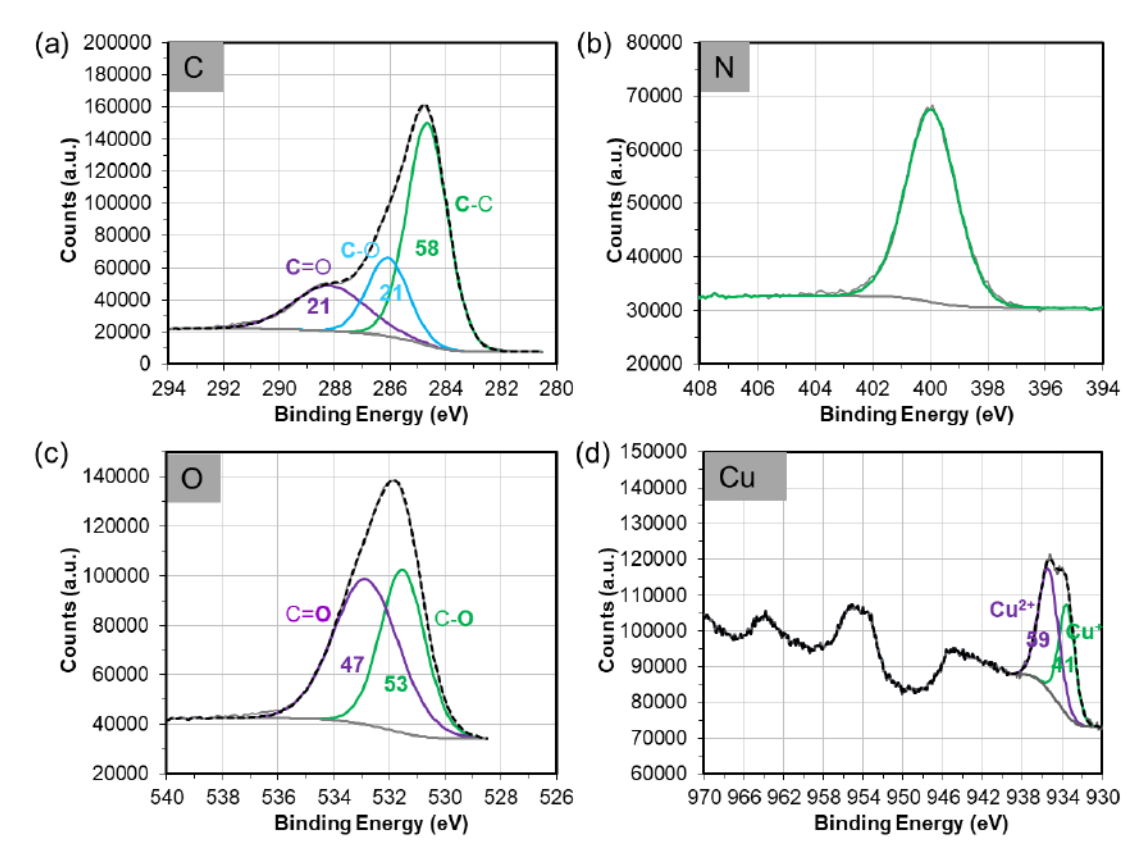


Figure S10. High resolution XPS spectrum of Cu<sub>3</sub>(HHTN)<sub>2</sub>: (a) C 1s; (b) N 1s: (c) O 1s; (d) Cu 2p. The corresponding ratios of the deconvoluted peaks are color-coded.

The XPS spectra revealed the presence of C, O, and Cu, along with N elements in Cu<sub>3</sub>(HHTN)<sub>2</sub> (**Figure S9**) in an elemental content of 69.5%, 15.7%, 7.4% and 7.5%, respectively.

High-resolution scans of the O 1s showed three peaks with binding energies at 284.7 eV, 286.2 eV, and 288.1 eV (Figure S10a), which can be ascribed to carbon in the environments of C-C, C-O, and C=O. The 1:1 intensity of the C-O to C=O indicated that the oxidation state of the ligand is tri(semiquinone). This analysis is consistent with the analysis of the high-resolution scan of O 1s range, which can be fitted to two peaks for C-O and C=O at binding energies of 531.5 and 532.9 eV in an intensity ratio of 48:52 (Figure S10c). The high-resolution scan of Cu 2p range can be deconvoluted two components at binding energies of 933.5 and 935.3 eV with an intensity ratio of 41:59, indicating that Cu in Cu<sub>3</sub>(HHTN)<sub>2</sub> exist as a mixed state of Cu(I) and Cu(II). Through deconvolution of the Cu 2p3/2 peak, the ratio of Cu(I) and Cu(II) in the framework is 41:59 (Figure 10d), close to a ratio of 2:3. Combing the above analysis, the skeleton of the MOF with a formula Cu<sub>3</sub>(HHTN)<sub>2</sub> will give a net charge of nearly -1. The counter ions for the compensation of the negative change of the framework are very likely from the NH<sub>4</sub>+, as suggested by the presence of N by XPS (Figure S10b).

#### 5. Structure Analysis by Computational Study and Powder X-ray Diffraction

To generate the cell parameters of the Cu<sub>3</sub>(HHTN)<sub>2</sub> MOF, a model structure which is composed of two trinaphthylene units, five Cu ions, and four hydrogen-terminated benzene units were built and then optimized at B3LYP/6-31G level. The optimized geometry of model molecular fragments used to generate the unit cell of the crystal is shown in **Figure S11**.

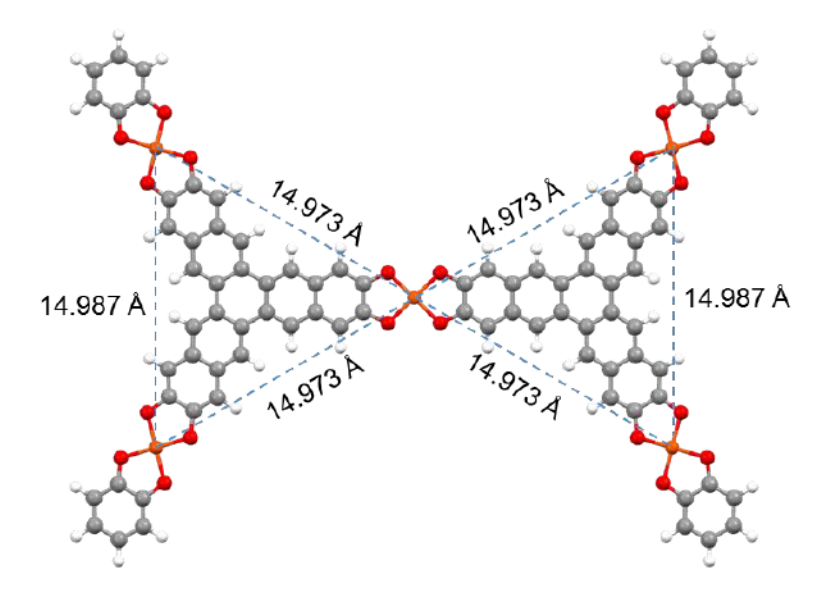


Figure S11. The optimized geometry of model molecular fragment used to generate unit cell of Cu<sub>3</sub>(HHTN)<sub>2</sub>.

In the optimized geometry, five Cu atoms formed two pseudo-isosceles triangles (side length difference < 0.1%). This structure was then introduced into Materials Studio Visualizer and converted into fractional coordinates using cell length a = b = 29.946 Å which was determined from the metal-metal distances of the above molecular fragment. An interlayer spacing of 3.29 Å was used which was the value calculated from the PXRD signal. The symmetry of the unit cell was found and forced into P6/mmm with a threshold of 1.0 pm (fine level). The geometry optimization including energy minimization with cell parameters was performed by using the CASTEP module in Materials Studio with Perdew–Burke–Ernzerhof (PBE) generalized gradient approximation (GGA) with a cut-off energy of 400.0 eV. The total energy change is set to less than  $10^{-5}$  eV and the magnitude of the largest force acting on the atoms is set to less than 0.03 eV A<sup>-1</sup>. After the optimization, a structure with of cell parameter of a=b=29.45 Å, c=3.29 Å in fully eclipsed packing was obtained.

To determine the displacement of the layer in structure with slipped-parallel packing, 66 different unit cells for parallel-displaced structures were generated from the grid of translations in the *ab*-plane (**Figure S12**) on the basis of the optimized model with fully eclipsed packing. The *c* value was doubled to 6.58 Å to accommodate two layers that are separate by 3.29 Å. Single-point energy calculations based on molecular force field COMPASS II (ultra-fine level) were carried out on these 66 structures using FORCIET modular implemented in Materials Studio. Single points energies at different translational positions were recorded. Plotting these energies values with the translation values along the *ab*-plane gives the contour map shown in **Figure S13**. The minimum of the potential energy surface corresponds to a displacement of ~1.4-1.5 Å along the *a/b* axis and ~0.7-0.8 Å along the *b/a* axis. The optimized crystal structure of Cu<sub>3</sub>(HHTN)<sub>2</sub> with the lattice parameters shown in **Figure S16**. Modeling of the staggered structures was performed in a similar manner but with the space group P63/mmc (**Figure S17**).

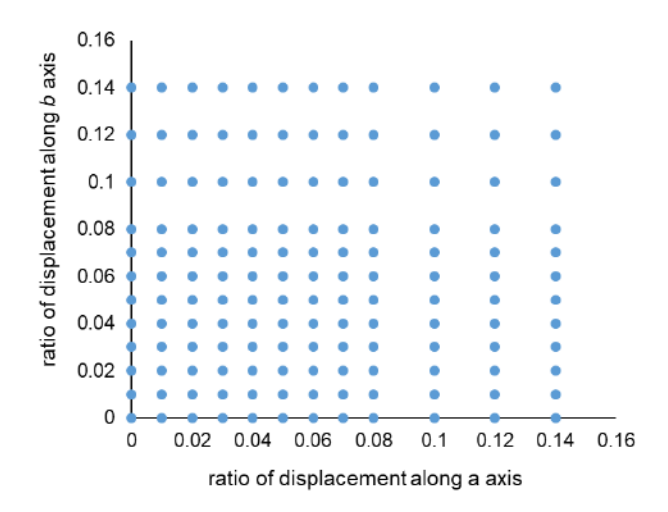
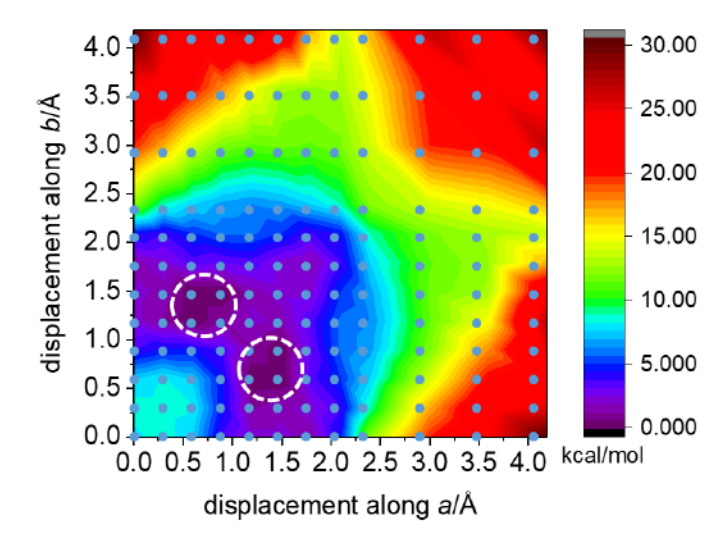
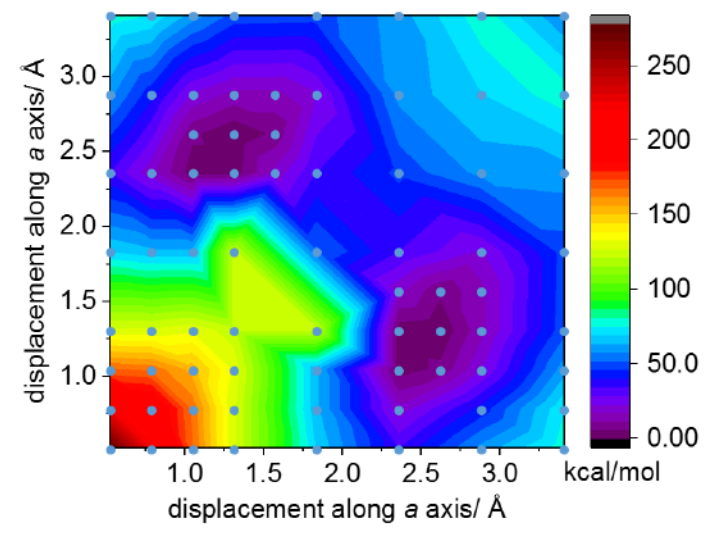


Figure S12. The grids of coordinate translations in the ab-plane that were sampled for single-point energy calculation.



**Figure S13**. Contour map of the potential energy surface for MOF  $Cu_3(HHTN)_2$  generated by different translations along a and b axis. The energy per unit cell at the minimum has been normalized to zero.



**Figure S14**. Contour map of the potential energy surface for  $Cu_3(HHB)_2$  generated by different translations along a and b axis. The energy per unit cell has been normalized to zero at the minimum.

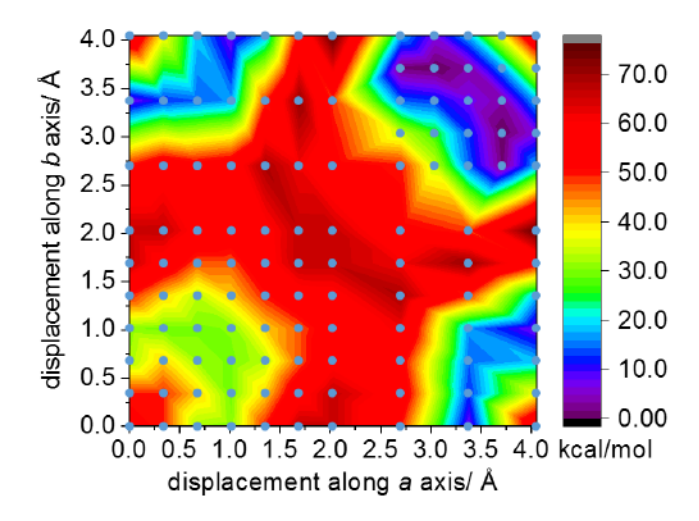
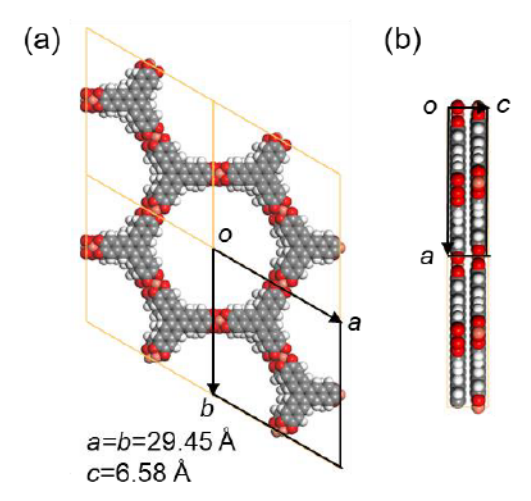


Figure S15. Contour map of the potential energy surface for  $Cu_3(HHTP)_2$  generated by different translations along a and b axis. The energy per unit cell has been normalized to zero at the minimum.



**Figure S16**. (a) Front and (b) side view of optimized Cu<sub>3</sub>(HHTN)<sub>2</sub> crystal structures with eclipsed packing mode and the corresponding cell parameters.

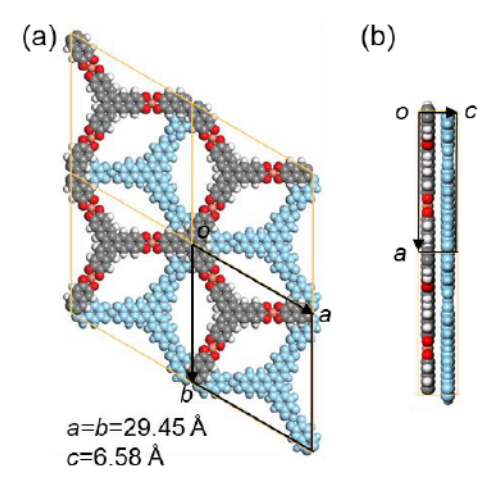
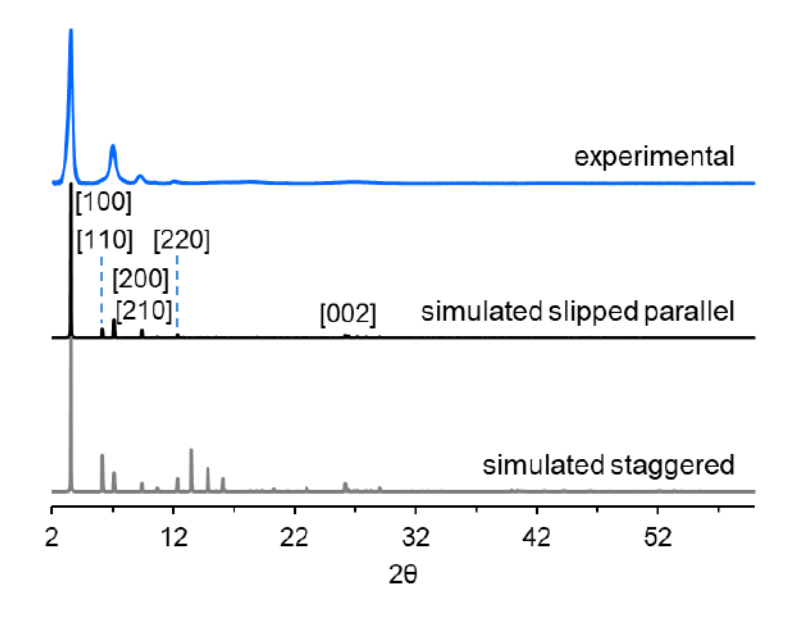


Figure S17. (a) Front and (b) side view of optimized Cu<sub>3</sub>(HHTN)<sub>2</sub> crystal structures with staggered packing mode and the corresponding cell parameters.

Powder X-ray diffraction (PXRD) data of  $Cu_3(HHTN)_2$  was collected using a Rigaku sixth generation MiniFlex X-ray diffractometer. Cu K $\alpha$  radiation ( $\lambda$  = 1.5406 Å; 600 W, 40 kV, 15 mA) was focused using a planar Göbel mirror riding the K $\alpha$  line.



**Figure S18**. Experimental (green line, corresponding to the sample obtained from **entry 9** in **Table S1**) and simulated PXRD pattern (black line) of MOF Cu<sub>3</sub>(HHTN)<sub>2</sub> in a slipped-parallel packing mode.

#### 6. SEM and TEM

Scanning electron microscopy of the MOF  $Cu_3(HHTN)_2$  was obtained using a Hitachi TM3000 SEM. The material was pressed onto carbon conductive tape that was attached to the aluminum plate. The images were taken at a 7 mm working distance using a 20 kV beamline in a to  $10^{-6}$  torr vacuum chamber.

Transmission electron microscopy was carried out in a Tecnai F20ST FEG TEM instrument. The sample was prepared by drop casting an acetone suspension (0.5 mg in 5 mL) of the MOFs onto a copper grid (300 mesh, 3.0 mm O.D). An operating voltage of 120 kV was used for imaging.

Energy dispersive X-Ray spectroscopy was collected using SDD X-ray microanalysis system with Octane Pro 10 sq. mm detector and TEAM software.

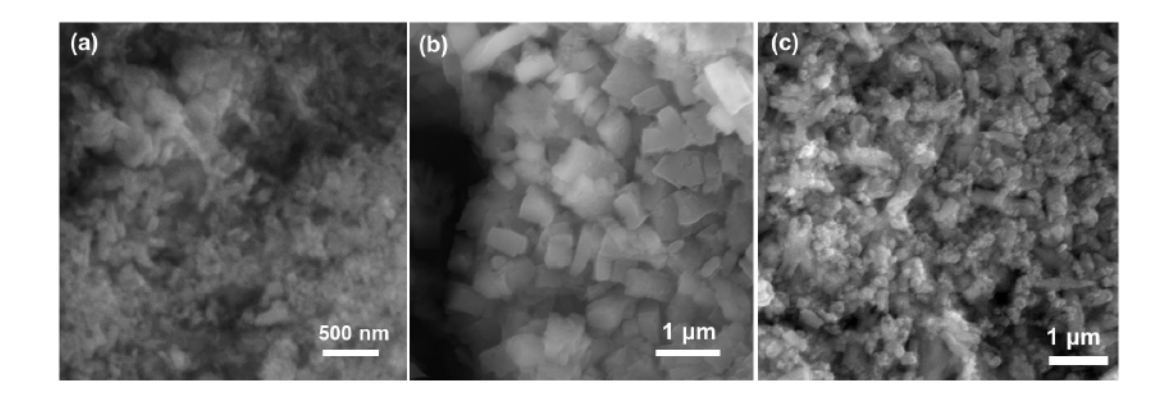


Figure S19. SEM image of MOF Cu<sub>3</sub>(HHTN)<sub>2</sub> under conditions as demonstrated in entry 8, 9, and 15 in Table S1.

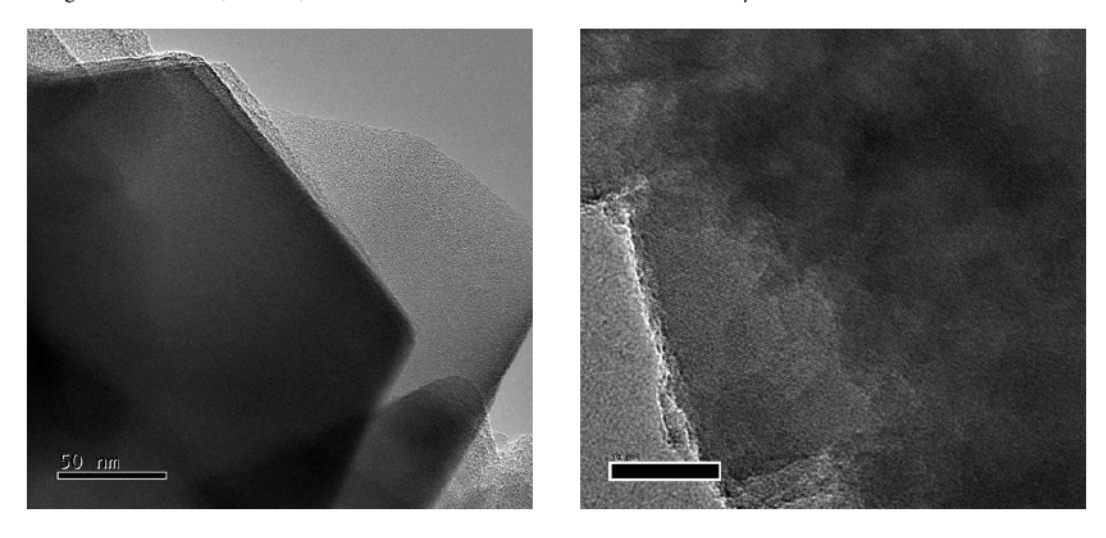


Figure S20. TEM image of MOF Cu<sub>3</sub>(HHTN)<sub>2</sub> under different magnifications.

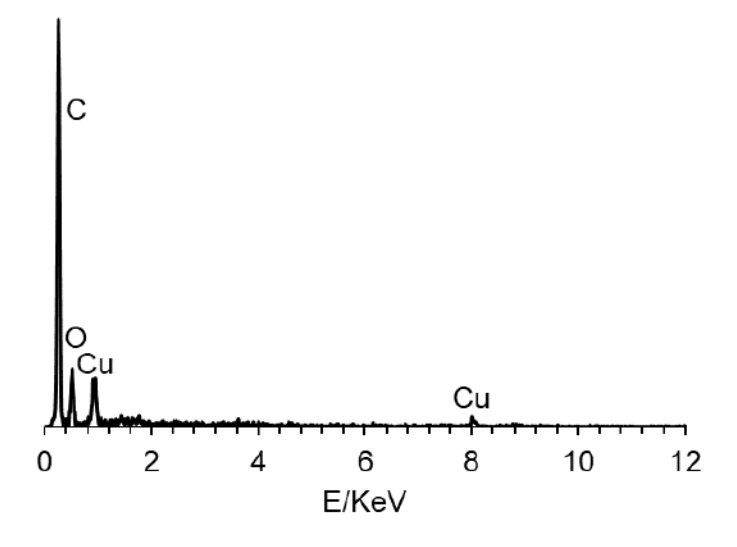


Figure S21. EDAX spectra of MOF Cu<sub>3</sub>(HHTN)<sub>2</sub> which show the existence of C, O, and Cu.

#### 7. Electron Paramagnetic Spectroscopy (EPR)

Since the HHTN theoretically has up to seven different oxidation states, low-temperature EPR studies of HHTN and  $Cu_3(HHTN)_2$  were performed to investigate the oxidation state of HHTN in the framework structure. The samples (~ 2 mg for each) were transferred to

an EPR tube. EPR spectra were collected on a Bruker BioSpin Gmbh spectrometer equipped with a standard mode cavity. The EPR spectrum was collected under liquid nitrogen temperature with the parameters listed in **Table S2**. The results showed that the HHTN ligand, which probably in its partially oxidized form, showed a very intense peak at g = 1.98938. Cu<sub>3</sub>(HHTN)<sub>2</sub> showed a strong peak at g = 2.07259, characteristic of an unpaired electron localized on the metal center.

Table S2. Parameters of EPR for samples HHTN and Cu<sub>3</sub>(HHTN)<sub>2</sub>.

Sample	sweep width/G	center field/G	modulation amplitude/G	microwave frequency/GHz	microwave power/mW
HHTN	1000	3500	4	9.771	0.2026
$Cu_3(HHTN)_2$	2000	3300	4	9.663	0.0638

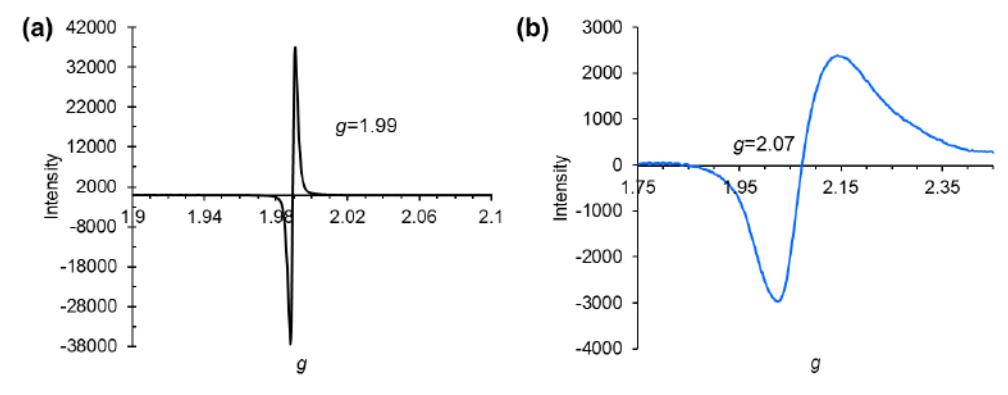


Figure S22. EPR spectrum of HHTN ligand and  $Cu_3(HHTN)_2$  MOFs. (a) The spectrum of the partially oxidized ligand HHTN which showed a g value factor at 1.98938. (b) EPR spectrum of the MOFs  $Cu_3(HHTN)_2$  showed a strong peak at g=2.07259.

#### 8. Thermal Gravimetric Analyses (TGA)

The thermal stability of the MOFs was investigated by thermal gravimetric analysis. Thermogravimetric analysis was performed in a TGA Q50 V5.0 instrument under nitrogen with a heating rate of 20 °C/min. The TGA curves demonstrated that before the temperature reached 130 °C, there is about 4% weight loss for Cu<sub>3</sub>(HHTN)<sub>2</sub>, which can be ascribed to the physically adsorbed solvent molecules. Followed by that, about 25% weight loss happened when the temperature was raised to 279 °C.

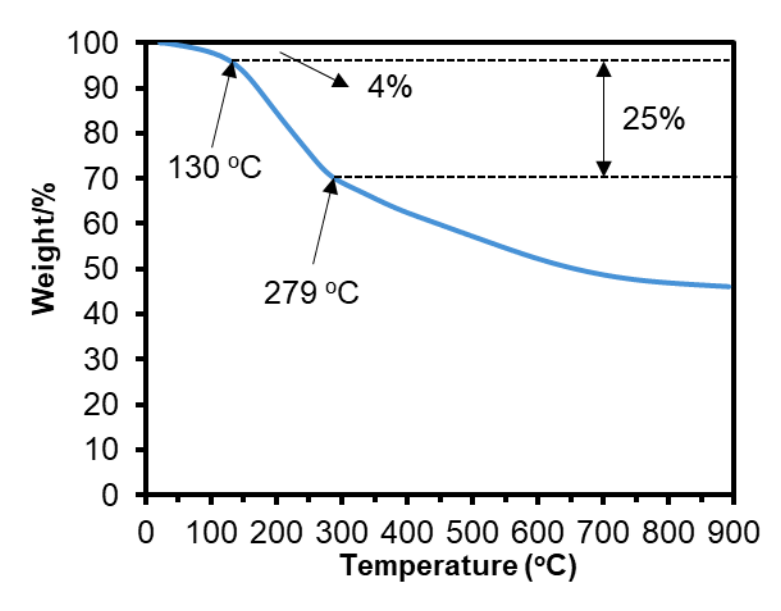


Figure S23. TGA curve of MOF Cu<sub>3</sub>(HHTN)<sub>2</sub>.

#### 9. Brunauer-Emmett-Teller (BET) Analysis

In order to assess the porosity and the architectural stability of MOF Cu<sub>3</sub>(HHTN)<sub>2</sub>, N<sub>2</sub> gas adsorption measurements at 77 K were performed. Before the gas adsorption test, the as-synthesized MOF was soaked in acetone for 2 days, during which the acetone was changed every 12 hours. The sample was then treated by using a supercritical CO<sub>2</sub> drier (Samdri'-795) with six times of "cool-fill-purge-heat-bleed-vent" cycle, in which the time for purge procedure was set to 45 min each time. Before gas adsorption measurement, the sample was further degassed under vacuum at 70 °C for 18 hours. For BET calculations, a full isotherm with a fitting range of 0 to 0.3 P/P<sub>0</sub> was used. The Brunauer-Emmett-Teller (BET) surface areas for Cu<sub>3</sub>(HHTN)<sub>2</sub> was calculated to be 486 m<sup>2</sup> g<sup>-1</sup>.

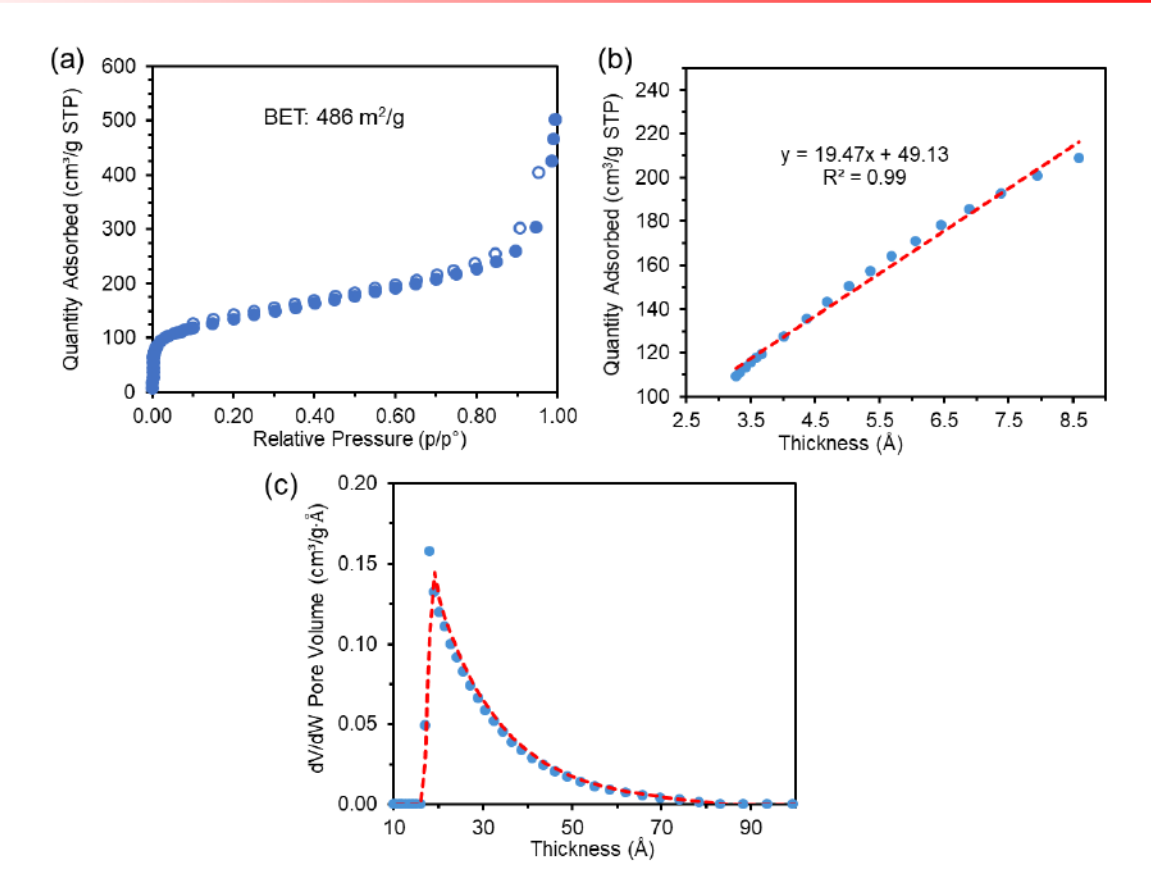


Figure S24. (a) Nitrogen sorption curves (filled circles: adsorption, open circles: desorption, STP=standard temperature pressure) and (b) t-Plot for nitrogen adsorbed at 77 K by activated Cu<sub>3</sub>(HHTN)<sub>2</sub>. The BET surface area by the gas adsorption analysis is 486 m<sup>2</sup>/g. The external surface area is 301 m<sup>2</sup>/g and the micropore area is 185 m<sup>2</sup>/g. (c) Pore size distribution.

#### 10. Measurement of Conductivity

To make a pressed pellet, ~45 mg of the MOF sample was put into a 6 mm inner-diameter split sleeve pressing die and pressed for 5 min under a pressure of approximately 1000 psi. A two-contact probe method was employed to collect bulk conductivity measurements of the MOFs pellet. The two-contact probe method is easy to configure and is suitable for the conductivity measurement of resistive samples.<sup>3</sup> We calculated the bulk conductivity measurements (S/cm) using **Equation S1**. Herein, L (0.091 cm) is the distance of between the probes which equals the thickness of the pallet, A is the basal area of the pellet, V (4 volts) is the voltage of cross the probes, I (A) is current which is measured by a potentiostat (Ivium CompactStat).<sup>4</sup>

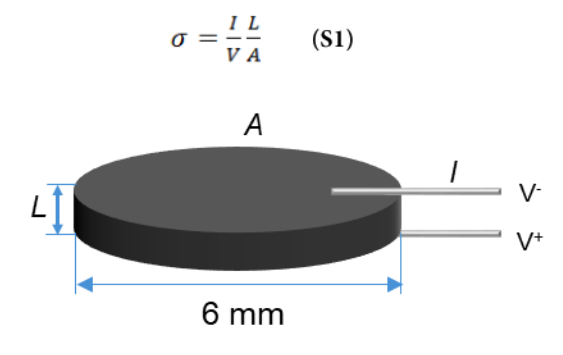


Figure S25. Representation of configuration for the measurement of conductivity by two-contact probe method.

To investigate the activation energy for electrical conductivity of Cu<sub>3</sub>(HHTN)<sub>2</sub>, conductivity of the pellet was measured under different temperatures from 298 K to 385 K with a constant applied voltage of 4.0 V. The conductivity values under different temperature are shown in **Figure S26**.

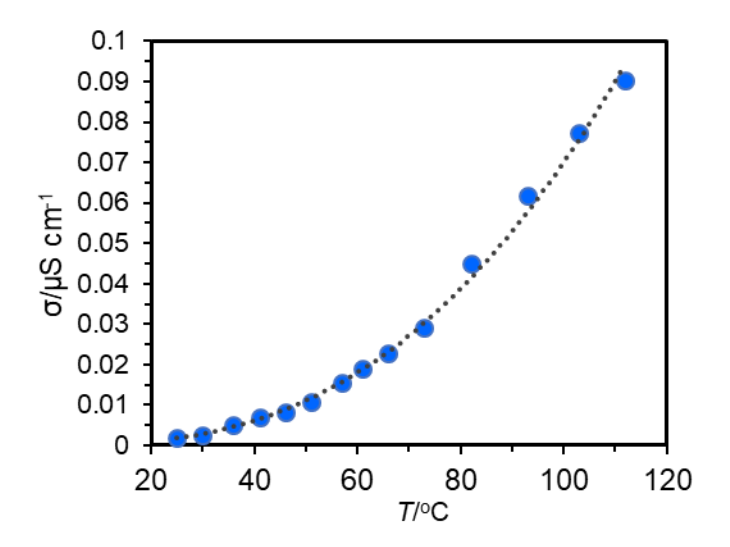


Figure S26. Conductivity of Cu<sub>3</sub>(HHTN)<sub>2</sub> measured as a function of temperature.

The Arrhenius equation,

$$\sigma = \sigma_0 e^{-\frac{E_a}{k_B T}}$$
 (S2)

can be used to access the activation energy. St In this equation,  $\sigma$  is the conductivity (S/cm),  $\sigma_{\theta}$  is the pre-exponential factor and is constant,  $E_a$  is the Arrhenius activation energy (kJ/mol),  $k_B$  is the Boltzmann constant (1.380649×10<sup>-23</sup> J/K), and T is the temperature (K). Taking the natural logarithm of Arrhenius equation yields:

$$ln(\sigma) = ln(\sigma_0) - \frac{1}{T} \frac{E_a}{k_B}$$
 (S3)

where  $\ln(\sigma_0)$  is a constant. The plot of the natural log of  $\ln(\sigma)$  to reciprocal temperature (1/T, in K<sup>-1</sup>) generates the value  $-\frac{E_a}{k_B}$ .

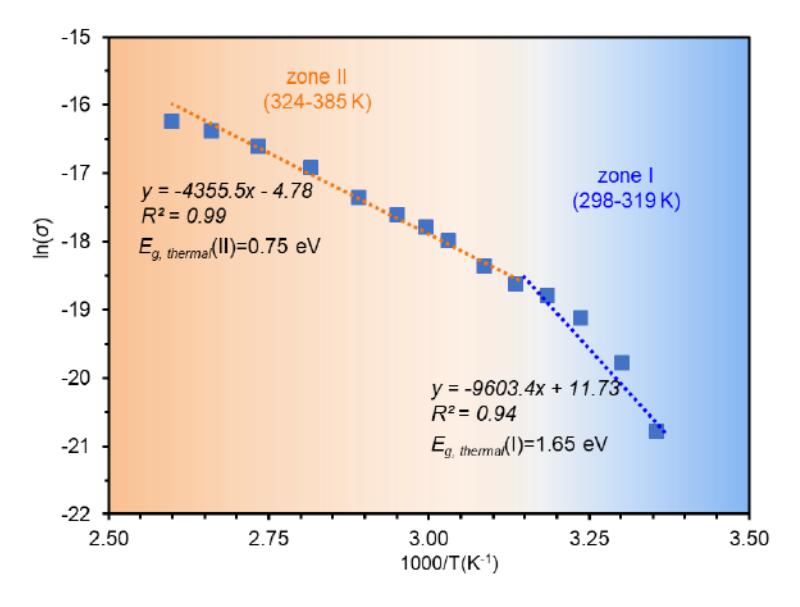


**Figure S27**. The plot of the natural log of conductivity vs temperature.

#### 11. I<sub>2</sub> Doping Study of Cu<sub>3</sub>(HHTN)<sub>2</sub>

Iodine-doped sample was carried out by heating 30 mg of Cu<sub>3</sub>HHTP<sub>2</sub> obtained from **entry 9** with 15 mg of I<sub>2</sub> in a sealed glassy vial at 40 °C for 12 h. The sample was cleaned by repeatedly immersing the sample into acetone and decanting the solution until the solution became colorless. The sample was further dried using an oil pump under room temperature for 1 day before the use for PXRD, EPR, and XPS study.

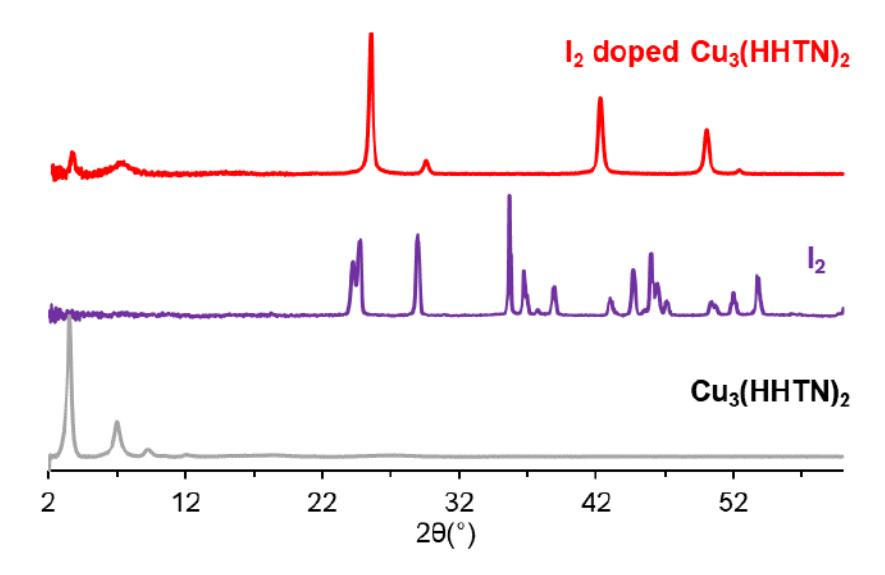


Figure S28. Experimental PXRD pattern of pristine MOF Cu<sub>3</sub>(HHTN)<sub>2</sub>, I<sub>2</sub>, and I<sub>2</sub> doped MOF Cu<sub>3</sub>(HHTN)<sub>2</sub>.

As shown in **Figure S28**, the material treated with  $I_2$  exhibited two obvious peaks at  $2\theta$ =3.5° and 7.0°, that is consistent with the [100] and [200] peak of pristine  $Cu_3(HHTN)_2$ , indicating that  $I_2$  doped  $Cu_3(HHTN)_2$  sample still maintained the crystalline framework structure. In addition, we observed significant peaks appeared at  $2\theta$ =25.5°, 29.6°, 42.3°, 50.1°, 52.5°. Since these peaks are different from elemental  $I_2$  crystals, which may indicate that regular structures associated with  $I_2$  doping, such as  $I_3$ ° chains, may be formed in the channels of  $Cu_3(HHTN)_2$ .

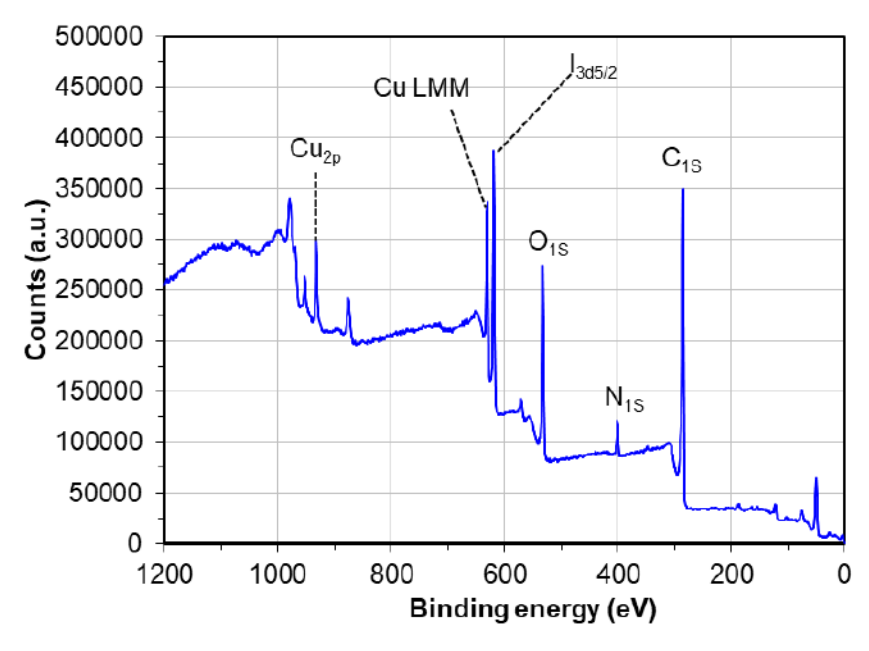
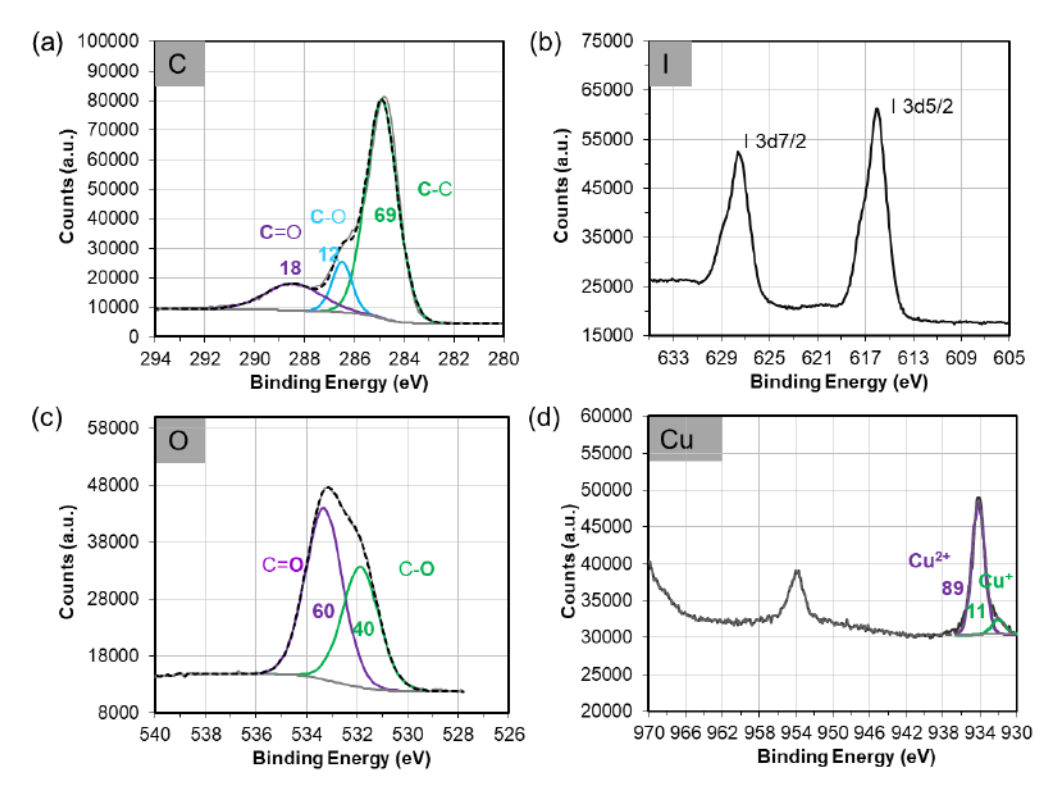


Figure S29. XPS survey spectrum of I<sub>2</sub> doped sample Cu<sub>3</sub>(HHTN)<sub>2</sub> showing the presence of C, N, O, I, Cu elements.



**Figure S30.** High resolution XPS spectrum of I<sub>2</sub> doped Cu<sub>3</sub>(HHTN)<sub>2</sub>: (a) C 1s; (b) I 3d: (c) O 1s; (d) Cu 2p. The corresponding ratios of the deconvoluted peaks are color-coded.

In the I<sub>2</sub>doped Cu<sub>3</sub>(HHTN)<sub>2</sub>, XPS spectra revealed the presence of C, O, N, Cu, and I in an elemental content of 56.1%, 16.0%, 3.7%, 5.3%, and 18.52 respectively (**Figure S29**). High-resolution scans showed that, after doping with I<sub>2</sub>, in the C 1s range the ratio of peaks at the binding energies of 285.5 eV, and 288.5 eV, corresponding to C-O and C=O, changed to 12:18 (**Figure S30a**). In the O 1s range, the intensity ratio of the two peaks for C-O and C=O at binding energies of 531.8 and 533.3 eV shifted to 40:60 (**Figure S30c**). Meanwhile, an obvious change in the Cu 2p3/2 area was also observed (**Figure S30d**). The two components at binding energies of 933.5 and 935.3 eV gave an intensity ratio of 89:11, corresponding to a Cu(II):C(I) ratio of ~9:1. The above results that, compared with pristine Cu<sub>3</sub>(HHTN)<sub>2</sub>, oxidation processes occurred at the probably both ligand and metal node. In addition, the high-resolution I 3d XPS spectrum showed two signals at 630.4 and 618.9 eV (**Figure S30b**), which respectively corresponded to I 3d7/2 and I 3d5/2 levels, suggesting the presence of I<sub>3</sub>-anions after iodine-doping.<sup>6</sup>

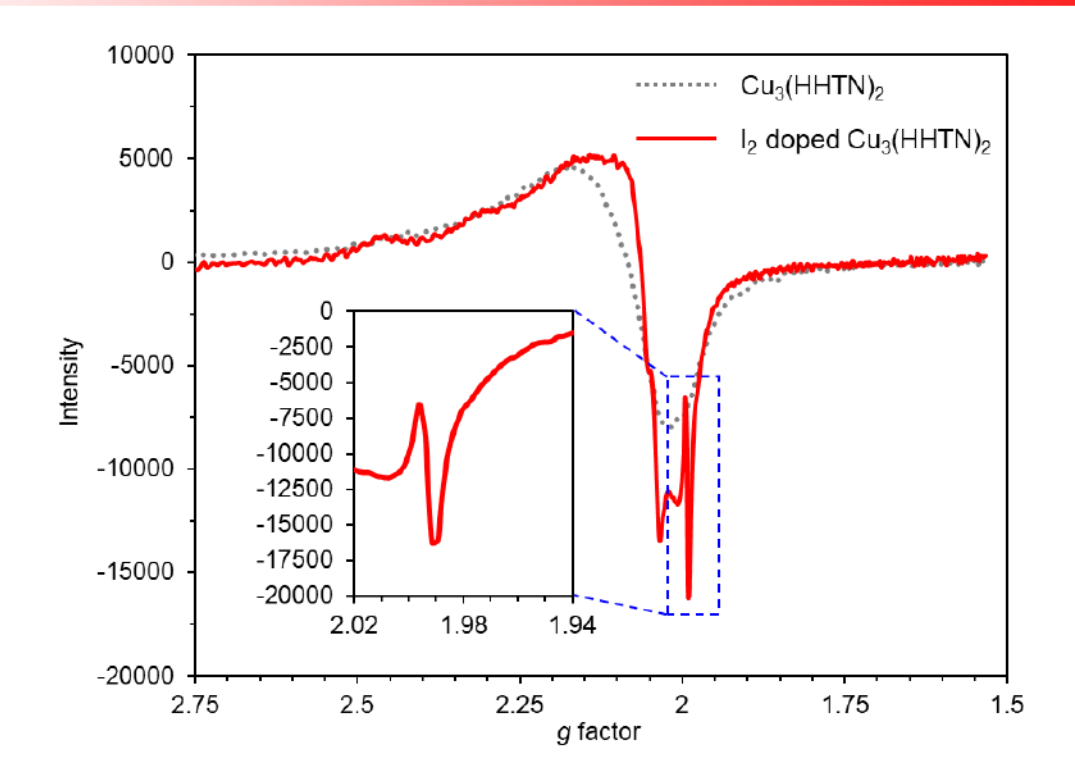


Figure S31. EPR spectra of pristine and iodine-doped Cu<sub>3</sub>(HHTN)<sub>2</sub> MOF.

In contrast to that of pristine  $Cu_3(HHTN)_2$  which showed only a broad signal with a g value at 2.073 (grey dash line, see also **Figure S22**), an additional EPR signal with a g value of 1.994 was observed for the iodine-doped  $Cu_3(HHTN)_2$  MOF (red solid line), indicating the formation of organic radicals due to ligand oxidation.<sup>6</sup>

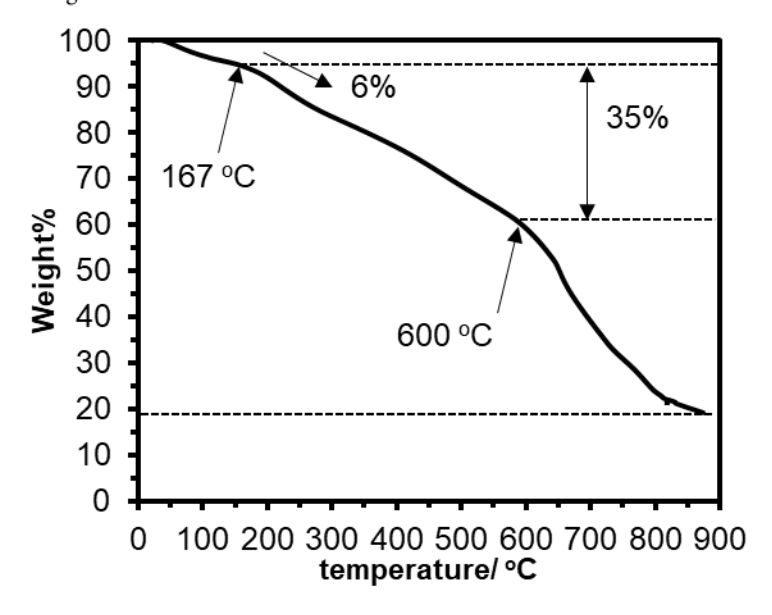


Figure S32. TGA curve of iodine-doped Cu<sub>3</sub>(HHTN)<sub>2</sub> MOF.

The I<sub>2</sub> doped Cu<sub>3</sub>(HHTN)<sub>2</sub> MOF exhibited a different TGA profile compared with pristine Cu<sub>3</sub>(HHTN)<sub>2</sub> MOF. When the temperature reached to 167 °C, there was about 6% weight loss for Cu<sub>3</sub>(HHTN)<sub>2</sub>, which can be ascribed to the physically adsorbed solvent molecules. Followed by that, about 35% weight loss happened when the temperature was raised to 600 °C. When the temperature got to 900 °C, a total weight loss of 80% was observed, vs 56% total weight loss observed for the pristine Cu<sub>3</sub>(HHTN)<sub>2</sub> at the same temperature (**Figure S23**). The

difference in a total weight loss of 24% is like ascribed to the doped I2, which is in a general agreement with that determined by XPS (19%).

For evaluating I<sub>2</sub> doping on the conductivity change of Cu<sub>3</sub>(HHTN)<sub>2</sub>, a Cu<sub>3</sub>(HHTN)<sub>2</sub> suspension in water (2 mg/mL) was drop casted onto a glass device equipped with interdigitated gold electrodes. The device was put into an I<sub>2</sub> atmosphere (concentration ~400 ppm)<sup>S7</sup> in a Teflon chamber under room temperature by using a similar method as previously reported. S8-9 The current of the device was monitored continuously by a potentiostat under a constant voltage bias of 4.0 V. The time-dependent study revealed that the current reached a maximal value after exposure to I<sub>2</sub> for 30 min with a 360-fold increase (Figure S33). The doping was partially reversible, as the current decreased to 157-fold of the initial value after the device was removed from the I<sub>2</sub> chamber and left under a continuous N<sub>2</sub> flow.

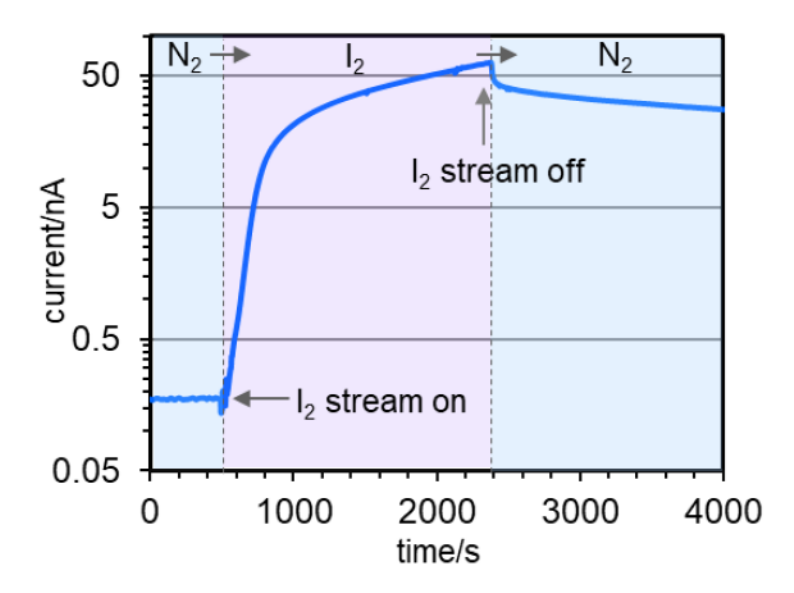


Figure S33. The change in the current of a resistor type device made of Cu<sub>3</sub>(HHTN)<sub>2</sub> upon I<sub>2</sub> doping.

#### References

- 1. Lynett, P. T.; Maly, K. E., Synthesis of substituted trinaphthylenes via aryne cyclotrimerization. Org. Lett. 2009, 11, 3726-9.
- 2. Rudiger, E. C.; Rominger, F.; Steuer, L.; Bunz, U. H., Synthesis of Substituted Trinaphthylenes. J. Org. Chem. 2016, 81, 193-196.
- 3. Sun, L.; Park, S. S.; Sheberla, D.; Dinca, M., Measuring and Reporting Electrical Conductivity in Metal-Organic Frameworks: Cd<sub>2</sub>(TTFTB) as a Case Study. *J. Am. Chem. Soc.* **2016**, *138*, 14772-14782.
- 4. Schroder, D. K., Semiconductor Material and Device Characterization. John Wiley & Sons, Inc.: 2005.
- 5. Darago, L. E.; Aubrey, M. L.; Yu, C. J.; Gonzalez, M. I.; Long, J. R., Electronic Conductivity, Ferrimagnetic Ordering, and Reductive Insertion Mediated by Organic Mixed-Valence in a Ferric Semiquinoid Metal-Organic Framework. *J. Am. Chem. Soc.* **2015**, *137*, 15703-15711.
- 6. Jiang, Y.; Oh, I.; Joo, S. H.; Buyukcakir, O.; Chen, X.; Lee, S. H.; Huang, M.; Seong, W. K.; Kwak, S. K.; Yoo, J. W.; Ruoff, R. S., Partial Oxidation-Induced Electrical Conductivity and Paramagnetism in a Ni(II) Tetraaza[14]annulene-Linked Metal Organic Framework. *J. Am. Chem. Soc.* 2019, 141, 16884-16893.
- 7. Baxter, G. P.; Hickey, C. H.; Holmes, W. C., The Vapor Pressure of Iodine. J. Am. Chem. Soc. 1907, 29, 127-136.
- 8. Wan, S.; Guo, J.; Kim, J.; Ihee, H.; Jiang, D., A belt-shaped, blue luminescent, and semiconducting covalent organic framework. *Angew. Chem. Int. Ed.* **2008**, *47*, 8826-30.
- 9. Cai, S.-L.; Zhang, Y.-B.; Pun, A. B.; He, B.; Yang, J.; Toma, F. M.; Sharp, I. D.; Yaghi, O. M.; Fan, J.; Zheng, S.-R.; Zhang, W.-G.; Liu, Y., Tunable electrical conductivity in oriented thin films of tetrathiafulvalene-based covalent organic framework. *Chem. Sci.* **2014**, *5*, 4693-4700.